Report on the numerical reservoir model used for the simulation of the Acoculco reservoir in Mexico

Deliverable 6.2

Report on the numerical reservoir model used for the simulation of the Acoculco reservoir in Mexico

Deliverable 6.2

Version 1.2

Paromita Deb, Dominique Knapp, Gabriele Marquart, Christoph Clauser

Contact: Paromita Deb (pdeb@eonerc.rwth-aachen.de)

RTWH Aachen

Work Package 6

02.04.2019

Website: http://www.gemex-h2020.eu

The GEMex project is supported by the European Union's Horizon 2020 programme for Research and Innovation under grant agreement No 727550

Table of Contents

List of figures

List of tables

Executive summary

Work Package (WP) 6 of GEMex project aims to characterise the superhot geothermal reservoir of Los Humeros and the engineered geothermal system (EGS) reservoir of Acoculco in terms of fluid and rock properties, heat transfer and flow conditions.

Both Acoculco and Los Humeros are situated in the Trans Mexican Volcanic Belt and are of high interest because of their unconventional geothermal characteristics. The geological situations of both of the fields are poorly understood and conceptual geological ideas are insufficiently defined. One of the main objectives within WP 6 is to have a better understanding of the fluid flow and heat transport conditions in both of the fields.

Acoculco is a geothermal prospective area hosted within the Tulancingo-Acoculco caldera complex. It has been categorised as a Hot Dry Rock System based on the temperatures encountered in the two exploration wells. Very high temperature and low permeability qualifies this zone as a potential target for an Enhanced Geothermal system (EGS).

This report describes the work done for simulating the natural state of thermal field of Acoculco. In addition, we analyse the performance of a potential geothermal doublet in terms of transient temperature and pressure variations. The structural geological model used for this purpose is created in WP 3. Uncertainties due to rock properties are evaluated by performing Monte Carlo simulations for static flow and thermal regimes. However uncertainties in the overall geometry of the caldera complex still prevails and the reader needs to keep this in mind before further use of the result presented here.

1 Introduction

The Acoculco geothermal zone is located at the eastern part of the Trans-Mexican volcanic belt and is around 140 km north-east of Mexico City. Geothermal manifestations in the form of extensive hydrothermal alteration, cold springs and gas discharges attracted the attention of the Mexican Federal Electricity Company (CFE) in this area (Lopez-Hernandez et al., 2009) which led to drilling of two exploration wells EAC-1 and EAC-2, 500 m apart from each other. The temperatures encountered in the wells are around 300 °C at a depth of 2000 m but negligible permeability was found. This led CFE to categorise this area as a Hot Dry Rock system (Pulido, 2010). Location of Acoculco area and the wells is shown in Figure 1.

2 Geological model

2.1 Geology

The Acoculco caldera complex is formed as a result of two main volcanic activities (Lopez-Hernandez et al., 2009). The oldest episode is referred to as Tulancingo Caldera and volcanic activity occured active between 3.0 Ma and 2.7 Ma. This outer caldera has a diameter of 32 km. A second caldera collapsed within this caldera and created Acoculco caldera with a dimeter of 18 km, associated with volcanic activity lasting from 1.7 Ma to 0.24 Ma.

The volcanic rocks of Acoculco rest on a sedimentary sequence consisting of folded Cretaceous limestones and shales belonging to the Sierra Madre Oriental (Lopez-Hernandez et al., 2009). On top of the sedimentary rocks several sequences of volcanic rocks are emplaced. Around the Acoculco caldera area porphyritic basaltic-andesitic lavas with phenocrysts of olivine and plagioclase and some dacitic domes are exposed originating from the Apan-Tezontepec Volcanic Field and the Apan-Tecocomulco Volcanic field (2.25 Ma ± 0.04 Ma to Holocene) and are related to the regional volcanic activity of the Trans Mexican Volcanic belt (Garcia-Palomo et al., 2002; García-Tovar et al., 2015; López-Hernández et al., 2009). Within the Acoculco caldera complex mainly basalts, basaltic trachy-andesites and rhyodacitic lava flows (with an age of 2.6 Ma – 2.2 Ma) can be found (Avellán et al., 2018a). At the margins of the Acoculco caldera several lava domes and flows and one ignimbrite layer, all of mainly rhyolitic composition (with an age of 2 Ma – 1 Ma) are buried by younger deposits (Sosa-Ceballos et al., 2018). The youngest volcanic events are of an age of 0.9 Ma – 0.06 Ma and consist of an ignimbrite deposit, rhyolitic domes and basaltic-andesitic cinder cones (Sosa-Ceballos et al., 2018).

Underneath Acoculco caldera, a hornblende granite intrusion emplaced within the cretaceous limestone sequence was cut by the two wells. The composition of rock samples and their ages (183 ±36ka) led to the interpretation of a young aplitic dike intrusion (or dike swarm) beneath Acoculco (Sosa-Ceballos et al., 2018). The result of this emplacement is a metamorphic contact aureole of skarn and marble rocks (Sosa-Ceballos et al., 2018).The main lithological units within the Acoculco caldera are interpreted based on the drilling data of the wells EAC-1 and EAC-2 (Figure 2).

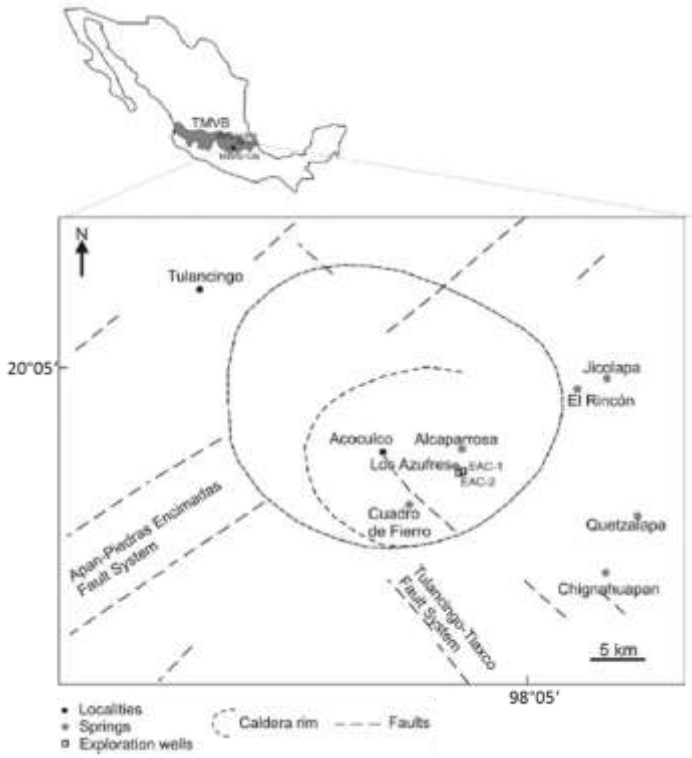

Figure 1: Location of the Acoculco caldera within the Trans Mexican Volcanic Belt; schematic of the Tulancingo-Acoculco caldera complex showing the caldera rim, the main fault systems, location of wells EAC-1 and EAC-2, springs and cities (Peiffer et al., 2014, Lopez-Hernandez et al., 2009)

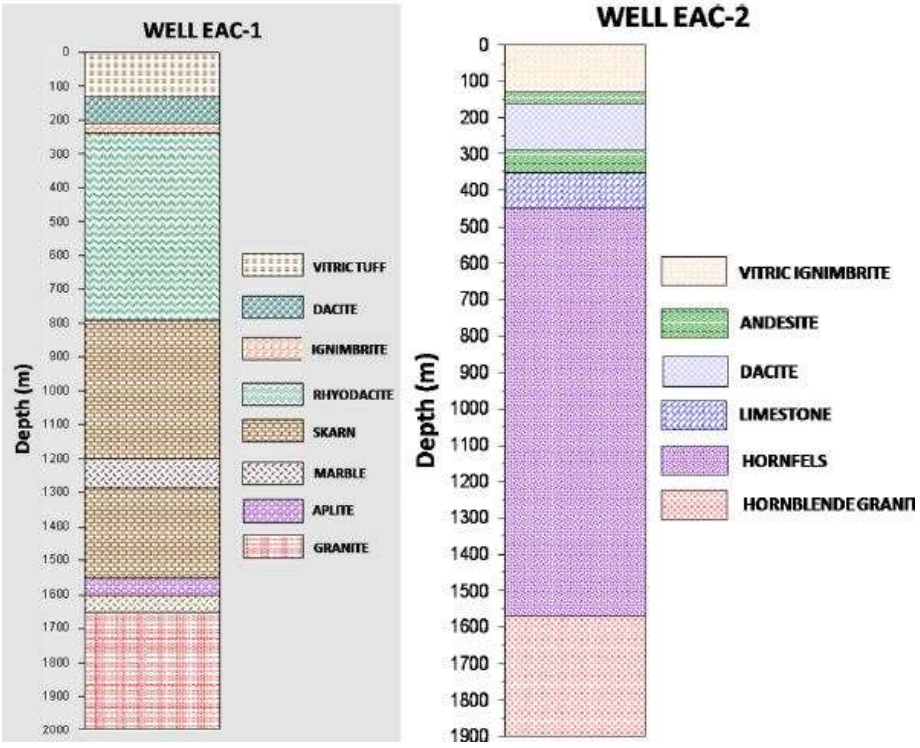

Figure 2: Lithology column of well EAC-1 and EAC-2 (Pulido, 2010), Skarn and Hornfels as classified by CFE in EAC-1 and EAC-2 respectively are both metamorphic rocks formed as a result of metasomatic processes in the host rocks due to igneous intrusions

2.2 Modeled units

The geological model used in WP 6 is provided by WP 3 and is based on Avellan et al. (2018). A detailed description of the Acoculco regional model is available in Calcagno et al. (2018). The regional model has a dimension of 55 × 37 × 6.5 km^3 and reaches a depth of 3 km below mean sea level. It consists of four major rock groups representing the major features of the Acoculco caldera system (Table 1). These groups comprise the sedimentary basement built up mainly of limestones, the granite intrusion emplaced within the basement, the metamorphic contact aureole made up of marble and skarns and the overlying, very heterogeneous group of pre-, syn- and post-caldera volcanites and alluvial deposits.

Table 1: Modelled units in GeoModeller (WP 3)

Unit	Rock description	Age
U1 Volcanites and alluvium	Rhyolitic ignimbrites and lava flows, andesites, basalts (pre-, syn and post-caldera), alluvial deposits	2.6 Ma to present
U2 Contact aureole	Marble and skarns, aplite dykes	2 – 1 Ma
U3 Granite intrusion	Hornblende granite	2 – 1 Ma
U4 Sedimentary basement	Jurassic and cretaceous limestones, argillite limestones, shales	140 – 250 Ma

The fault structures mapped in Acoculco are based on field work performed by EU and Mexican researchers within GEMex. Three different kind of faults are recognised: normal faults, damage zones and the caldera faults. The normal faults and the damage zones act as the main regional fault systems with mutual cross-cutting relationships. The caldera faults are considered as the gravitational local faults (WP 3 and WP 4, GEMex). These fault systems are also described in Lopez-Hernandez et al. (2009) and Peiffer et al. (2014). The faults considered in the model are shown in Figure 3.

3 Available data

3.1 Well data

Exploration wells EAC-1 and EAC-2 were drilled in 1995 and 2008, respectively, to access the potential of the Acoculco geothermal area. Both the wells are vertical, EAC-1 reaches a depth of 2000 m while EAC-2 has a total depth of 1900 m (Figure 2).

Temperature and pressure logging was performed in both EAC-1 and EAC-2 wells. The available data for EAC-1 includes temperature logs after 6, 12, 18 and 24 hours of drilling and pressure logs after 6 and 24 hours of drilling. Additionally, there were heating up surveys after 12 and 13 days of heating for both temperature and pressure. For EAC -2 well, the temperature logging is performed 6, 12, 18 and 24 hours after drilling while the pressure data available is logged after 18 and 24 hours of drilling.

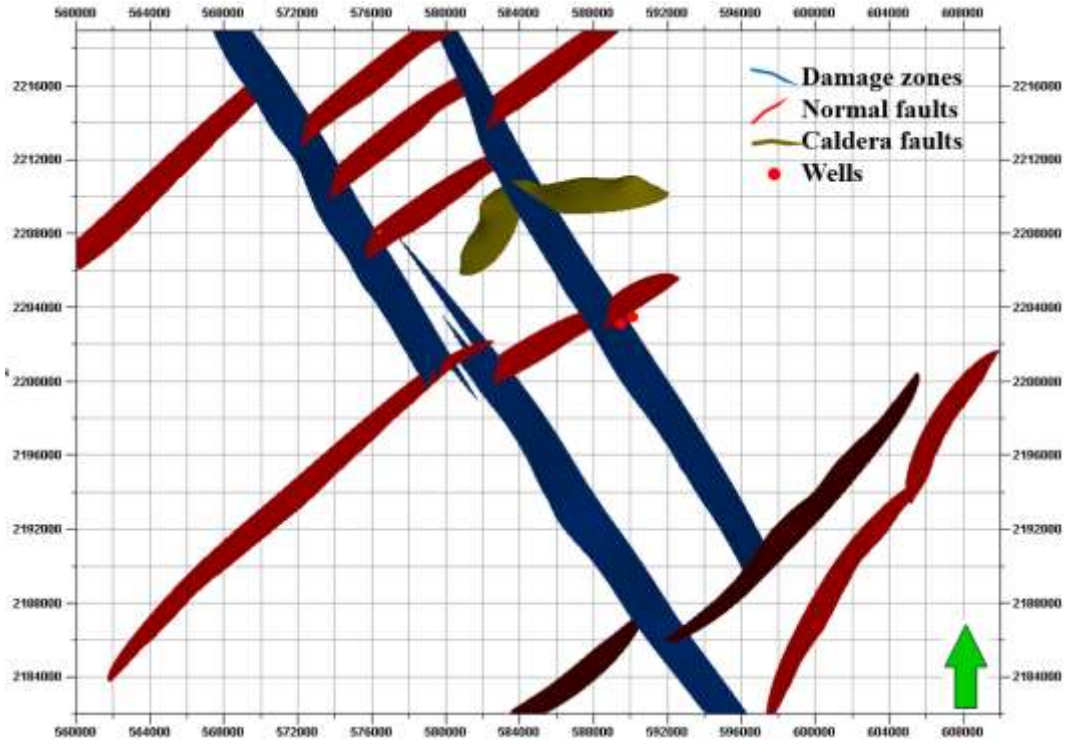

Figure 3: Modelled faults in Acoculco (WP 3, WP 4), NE-SW trending normal faults, NW-SE trending damaged zones and almost E-W trending caldera faults, EAC-1 and EAC-2 wells are indicated by the red dots

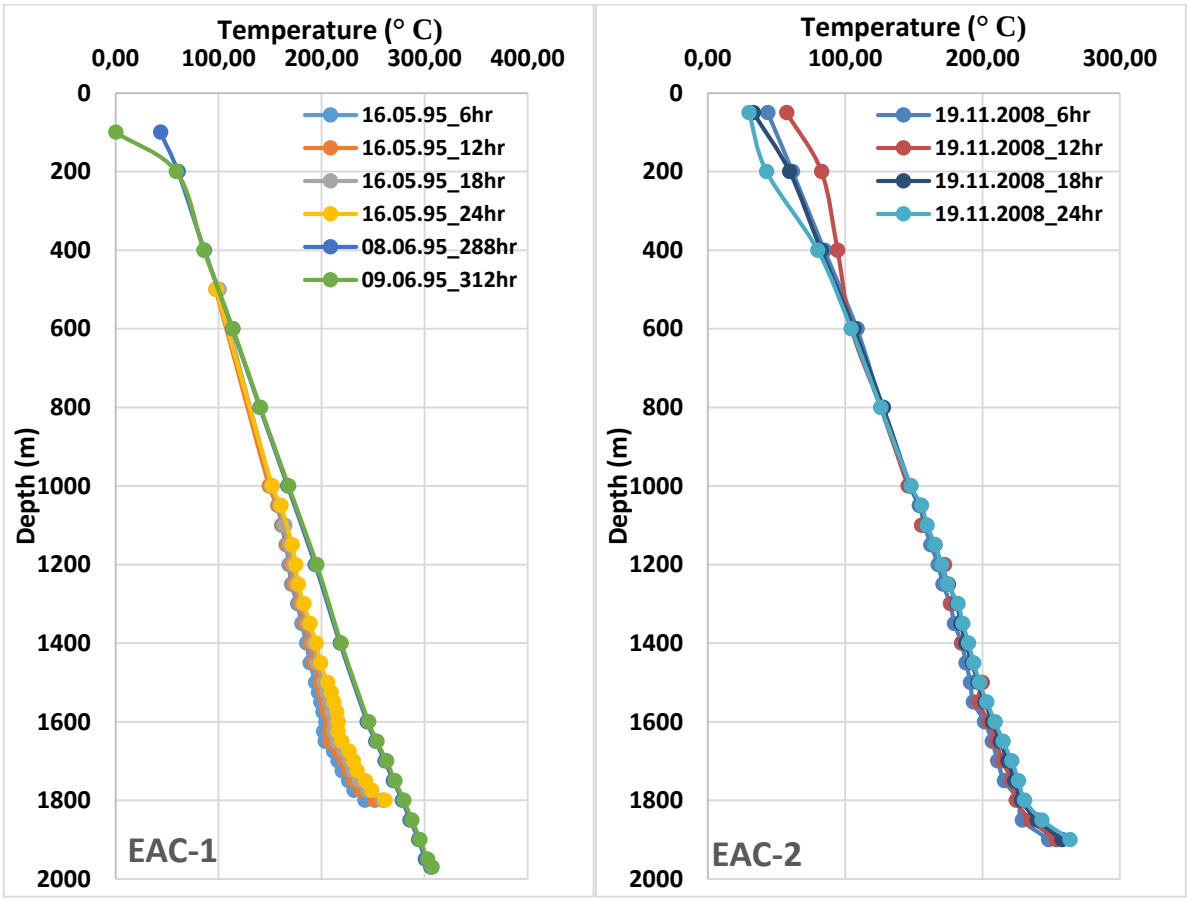

Figure 4: Temperature logs run at different dates for EAC-1 (left) and EAC-2 (right)

The temperature data from the heating up profiles logged on 08.06.95 and 09.06.95 for EAC-1 indicates that the well has reached stable condition. The temperature points used for calibrating the thermal model corresponds to the stable temperature profiles for both EAC-1 and EAC-2 and is presented in Table 2.

Table 2: Stabilised bottom hole temperatures (BHT) for EAC-1 and EAC-2

Wells	Depth (m)	Stabilized Temperature (°C)
EAC-1	1800	280.00
	1970	307.00
EAC-2	1900	270

3.2 Outcrop samples

Several field campaigns were conducted between January 2017 and May 2018 to collect representative samples from Los Humeros, Acoculco and the exhumed system, Las Minas. Details of the field campaign, description and physical condition of the samples, methodologies and measurements are described in Deliverable Report D 6.1. The reporting deadline for D 6.1 as well as D 6.2 and D 6.3 were identical. Considering this, it was decided to use measurements performed until November 2018 for petrophysical characterization.

4 Numerical Modelling

4.1 Mathematical equations

For numerical simulation the finite differences code SHEMAT-Suite (Rath et al., 2006) is used. SHEMAT–Suite is based on SHEMAT (Simulator for Heat and Mass Transport; Clauser, 2003) and solves the coupled steady state or transient equations for groundwater flow, heat and reactive solute transport. For our modelling of the natural state, we restrict ourselves to a steady state modelling of the initial temperature and pressure fields, due the unclear conceptual model ideas of the heat source and the lack of information corresponding to the cooling history, the position and the size of possible magma chambers or pockets, which are needed for performing a detailed transient modelling of the fields initial state.

The steady state mass conservation of water in a porous medium is expressed by the continuity equation, where h represents the hydraulic head, Q labels the source and sink term, $\boldsymbol{k}$ is the permeability tensor, ρ_f and μ_f are density and dynamic viscosity of the pore fluid, respectively and g is gravity acceleration:

$$\nabla\left(\frac{\rho_f g}{\mu_f}\boldsymbol{k}\,\nabla h\right) + Q = 0. \qquad (1)$$

The physical properties of water in sub-critical and super-critical conditions are calculated using the correlations provided by the International Association for the Properties of Water and Steam (Wagner et al., 2000). The pore water pressure (P) is calculated according to the head distribution and the depth z, given by the definition of de Marsily (1986), where P_0 represents the pressure at the surface for z=0:

$$P(z,h) = P_0 + \int_0^z \rho_f(\tilde{z}) g(h - \tilde{\tilde{z}}) d\tilde{z}. \quad (2)$$

Heat transport due to conduction, advection and radiogenic heat production is expressed in the energy conservation equation in steady state

$$(\rho c)_f \mathbf{v} \nabla \mathrm{T} - \nabla (\lambda_e \nabla T) = A. \quad (3)$$

The equation consists of an advective term, yielding Darcy velocity **v**, fluid density ρ_f and fluid specific heat capacity c_f, a diffusive term, comprising the effective thermal conductivity of the rock-fluid mixture λ_e and a heat production term A.

Groundwater flow and Darcy velocity **v** are described by the Darcy's Law:

$$\mathrm{v} = \frac{k}{\mu_f}(\nabla p - \rho_f g). \quad (4)$$

Rock thermal conductivity depends on the rock type but generally decreases with temperature (Zoth and Hänel, 1988). It is important to know the representative values of thermal conductivity with temperature and pressure for thermal modelling. The dominant part of the regional model is composed of limestone basement metamorphosed to skarn and marble in the contact aureoles. This is overlain by igneous and metamorphic rocks (pre-caldera and caldera deposits). Lee and Deming (1998) propose that the best theoretical fit for the thermal conductivity - temperature dependency of igneous and metamorphic rocks in the temperature range from 0 °C to 500 °C, compared to measured data is the relationship proposed by Sekiguchi (1984) (5). We used the correction proposed by Sekiguchi (1984) to account for the dominant igneous and magmatic rock compounds within the model domain.

The formula implements the temperature correction for matrix thermal conductivity λ_m on basis of a given matrix conductivity at room temperature $\lambda_{m,0}$ and the temperature T and was included in the manner of Pasquale et al. (2017):

$$\lambda_m = 1.8418 + (\lambda_{m,0} - 1.8418)\left(\frac{1}{0.002732\,T + 0.7463} - 0.2485\right). \quad (5)$$

Effective thermal conductivity of the fluid filled porous rock λ_e depends on porosity, ϕ , fluid thermal conductivity λ_f and rock matrix thermal conductivity λ_m. It is calculated according to the geometric mean (Clauser, 2003):

$$\lambda_e = \lambda_f^{\phi}\, \lambda_m^{(1-\phi)}. \quad (6)$$

For transient simulation in the stimulated reservoir volume, the following formulations are implemented.

The thermal power P_t [W] of the geothermal doublet installation is evaluated using the temperature at the producer T [°C]:

$$P_t = \rho_f c_p \, \Delta T \, Q. \tag{7}$$

With ρ_f as fluid density [kg m^{-3}] (assumed constant throughout our simulations to balance mass), c_p specific heat capacity of the fluid [J $kg^{-1}K^{-1}$] (constant value for calculations), $\Delta T = T_{Producer} - T_{Injector}$ is the temperature difference between produced and injected fluid [K] (in our case $\Delta T = T_{Producer} - 70°$ C) and Q is the production flow rate [m^3 s^{-1}]. It is assumed that there is no temperature drop while the produced water is ascending through the cooler rocks of the surroundings.

To calculate the pressure within the wells p_w we use the semi-analytical approach by Peaceman (1983) to convert the corresponding numerical grid block pressures p_b to well pressures:

$$p_w = p_b - \frac{q_w \mu_f}{2\pi k \Delta z} ln\left(\frac{r}{r_w}\right). \tag{8}$$

Given the flow rate q_w [m^3 s^{-1}], fluid dynamic viscosity μ_f [Pa s], permeability k [m^2], the vertical discretization of the corresponding grid cell in z-direction Δz [m] and the well radius r_w [m]. For the well radius 7.25 cm are assumed, this number corresponds to the completed well diameter of 5 5/7 inch in the two wells (Lorenzo Pulido et al., 2010). The parameter r is the equivalent radius of the cell. For a cubic cell with isotropic permeability, the original formulation by Peaceman (1983) can be simplified to

$$r = 0.14\sqrt{2}\Delta x. \tag{9}$$

where Δx corresponds to the grid cell discretization in x and y direction. For all reservoir models used Δx = 10 m and Δz = 20 m.

From the mean pressures at the injector and the producer, reservoir impedance, i can be calculated using the average pressures at the producer and injector and the production flow rate Q:

$$i = \frac{p_{injector} - p_{producer}}{Q}. \tag{10}$$

Reservoir impedance reflects the pressure difference needed to circulate a fluid volume through the stimulated permeable zone (Kolditz and Clauser, 1998). The reservoir impedance should not exceed 100 kPa s L^{-1} to ensure economic feasibility of the project (Clauser, 2006).

4.2 Parameterization

The structural geological model of Acoculco caldera was populated with physical properties using the laboratory data from outcrop and reservoir samples obtained from laboratory measurements performed in Task 6.1. Missing values for rocks which have not been sampled have been compiled from literature. For Unit 1 (Volcanites), which is composed of heterogeneous volcanic successions, the relative contributions of

the dominating rock types (rhyolitic ignimbrites, andesites, basalts) were calculated by their volume fractions recovered from their thicknesses from the wells. In absence of any other subsurface information to define the spatial distribution of the rock types, the proportions obtained from wells were used for the entire model. From the well lithological record, rhyolitic ignimbrites and minor rhyolitic lavas contribute with a thickness of about 400 meters to the overlying unit. The andesites encountered make up to 300 m and the basalts make up to 200 m in thickness (Information WP 3). The total thickness of the volcanite unit is only up to 500 m and its composition changes spatially. The rhyolitic ignimbrites contribute 44 %, the andesites contribute 33 % and the basalts 23 % to Unit 1. From the conceptual model, skarn and marble are the main lithology building up Unit 2. The relative amount of the rock masses is assumed to be 80 % marble and 20 % skarn. This differentiation is not based on well data but rather an assumption based on conceptual idea assuming several aplite dykes as the source of contact metamorphism, resulting in a direct contact product of skarn around the dyke and marble in the further surrounding. The underlying metamorphic basement composing mainly of phyllite was not included in the regional and local simulations due to absence of any information.

Table 3 shows the parameterization of the model units used for simulation. Coloured rows represent the final composition used for the mixed units of volcanites and marble & skarn. All values for the granite lithology as well as the values for the heat production rate are compiled from Schön (2004) and Rybach (1976, 1986).

Table 3: Parameterization of the modelled units based on laboratory and literature data

Units	Lithology	Porosity [%]			Matrix Thermal Conductivity $\left[\frac{W}{m\,K}\right]$			Permeability (matrix) [m²]			Heat Production Rate $\left[\frac{\mu W}{m^3}\right]$	Vol. Heat Capacity $\left[\frac{W}{m^3\,K}\right]$		
		Mean	Std.Dev.	N	Mean	Std.Dev	N	Mean	Std.Dev	N	Mean	Mean	Std.Dev	N
1a	Rhyolitic Ignimbrites	14.30	1.96	15	2.74	0.13	14	1.17E-17	6.96E-18	10	1.48	2117271	154843	5
1b	Andesites	6.00	1.73	-	2.42	0.26	16	1.06E-16	2.17E-16	6	1.08	2134740	142902	29
1c	Basalts, Rhyodacites, Andesites, Olivine Basalts	12.80	2.60	19	2.18	0.23	11	1.18E-15	2.78E-15	16	0.5	2035034	79063	2
1	**Volcanites**	**11.20**	**2.02**	**-**	**2.50**	**0.19**	**-**	**3.03E-16**	**6.93E-16**	**-**	**1.13**	**2104819**	**134023**	**-**
2	**Limestones**	**1.17**	**1.40**	**32**	**2.90**	**0.26**	**25**	**2.02E-18**	**2.30E-18**	**17**	**0.62**	**2080855**	**16538**	**2**
3a	Marble	0.56	0.56	20	3.78	0.87	16	3.31E-18	4.79E-18	17	0.62	2336427	72451	2
3b	Skarn	3.84	0.78	8	4.34	0.14	8	1.86E-18	1.35E-18	8	0.62	2697363	47060	1
3	**Marble and Skarn**	**1.22**	**0.60**	**-**	**3.89**	**0.60**	**-**	**2.15E-18**	**2.04E-18**	**-**	**0.62**	**2625176**	**52138**	**-**
4	**Granite**	**2.00**	**-**	**-**	**3.20**	**-**	**-**	**3.00E-18**	**-**	**-**	**2.45**	**2730075**	**534374**	**-**

4.3 Regional Conductive model:

Temperature data from EAC-1 and EAC-2 indicated a high temperature and conductive gradient (Figure 4). Low permeability formation was inferred from the negligible circulation losses encountered in both the wells (Pulido et al., 2010). From core sample investigation of well EAC-1, intense hydrothermal alteration and mineral precipitation has been observed, which resulted in fracture self-sealing and inhibition of flow (López-Hernández et al., 2009). Within the limestone and skarn sections, intense intervals of fractures and micro fractures filled by calcite and pyrite precipitation have been reported (Lorenzo Pulido et al., 2010). The low permeability of the rocks encountered by EAC-1 is additionally enforced by the negligible intrinsic permeability of granite, marble and skarn and the lack of recent tectonic and magmatic activity (López-Hernández et al., 2009).

Based on these observations, we consider that the dominant process for heat transport is conduction. Regionally mineralisation has been observed in structures oriented along the NW-SE and NE-SW faults

indicating that the faults were active fluid pathways in the past (López-Hernández et al., 2009). Therefore, it can be expected that the dissolution channels and fracture networks existed in the limestone and the skarns which are now sealed as a result of mineralisation.

We therefore perform in a first step conductive simulations on the regional scale to evaluate the influence of the specific basal heat flow on the temperature profile of the wells. The regional model of Acoculco area comprises a size of 55 km × 37 km × 3.5 km and was discretized into equal cells of 250 m × 250 m × 50 m resulting in a total number of 2.3 million cells for the numerical grid. Conductive models with several basal heat flow scenarios are run as shown in Figure 5. The simulated temperature depth profiles at the positions of the wells are then compared with the BHT at particular depth to obtain an approximation of the basal heat flow conditions.

Boundary conditions:
The regional model boundary conditions have been chosen with respect to topography. At the top of our model domain, temperature is assigned dependent on altitude as a Dirichlet boundary condition, coinciding with the ground surface. As a reference point the annual mean air temperature of 12 °C measured at Acoculco climate station situated at an elevation of 2779 m.a.s.l. was used. As no soil temperature is available from the station data, the boundary condition of temperature at the ground surface is calculated from the mean annual air temperature and the topographic height, assuming ground surface and air temperature has the same gradient.

The average specific heat flow obtained from borehole data in the TMVB and Sierra Madre Oriental is 90 mW m^{-2} (± 16 mW m^{-2}), (Ziagos et al., 1985). Other authors state the specific heat flow in the area to range between 75 mW m^{-2} and 83 mW m^{-2} (Pollack et al., 2010) or even 35 mW m^{-2} and 85 mW m^{-2} (Davies, 2013). This observed high variability of the heat flow distribution on a larger scale can be explained by the complex setting of the continental trench-arc-back arc system and the temperature perturbations due to uplift, orogeny and erosion (Ziagos et al., 1985). From the stabilized temperature log of EAC-1, the geothermal gradient calculated within the granite is 0.166 K m^{-1}. Assuming a bulk thermal conductivity, λ_{bulk} of the granite within the range of 2.0 W $m^{-1}K^{-1}$ to 3.0 W $m^{-1}K^{-1}$, the heat flow q within the granite strata can be calculated using Fourier's law:

$$q = -\lambda_{bulk} \frac{\partial T}{\partial z}. \tag{11}$$

This calculation results in a specific heat flow q ranging from 332 mW m^{-2} to 498 mW m^{-2}. It should be noted that rock thermal conductivity decreases with temperature. At the bottom hole of both wells temperatures up to 300 °C are obtained, this implies that the thermal conductivity of the rock will already be strongly decreased from the measured value at room temperature, resulting in a lower overall range with temperature at depth. This might change the 3D heat flow field and decrease the vertical heat flow.

To determine the specific heat flow signal of the granite intrusion, we iteratively upscale the specific heat flow boundary condition from 300 mW m^{-2} to 500 mW m^{-2} in the outlines of the intrusion at the bottom of our model domain (Figure 5) and compare the results to the bottom hole temperature data of the two wells (Figure 6). The surrounding regional heat flow is assigned to a constant value of 91 mW m^{-2} due to the lack of other temperature data and calibration points.

The result shows a good match of the bottom hole temperatures of EAC-1 with a specific heat flow of 400 mW m^{-2} whereas the temperatures of well EAC-2 match better with a specific heat flow of 350 mW m^{-2}. Although both wells are positioned only 549 m from each other and meet the same bottom hole lithology, the

difference in bottom hole temperature might be explainable by either a strongly deviating lithological composition or a different localised heat source, for example aplite dykes.

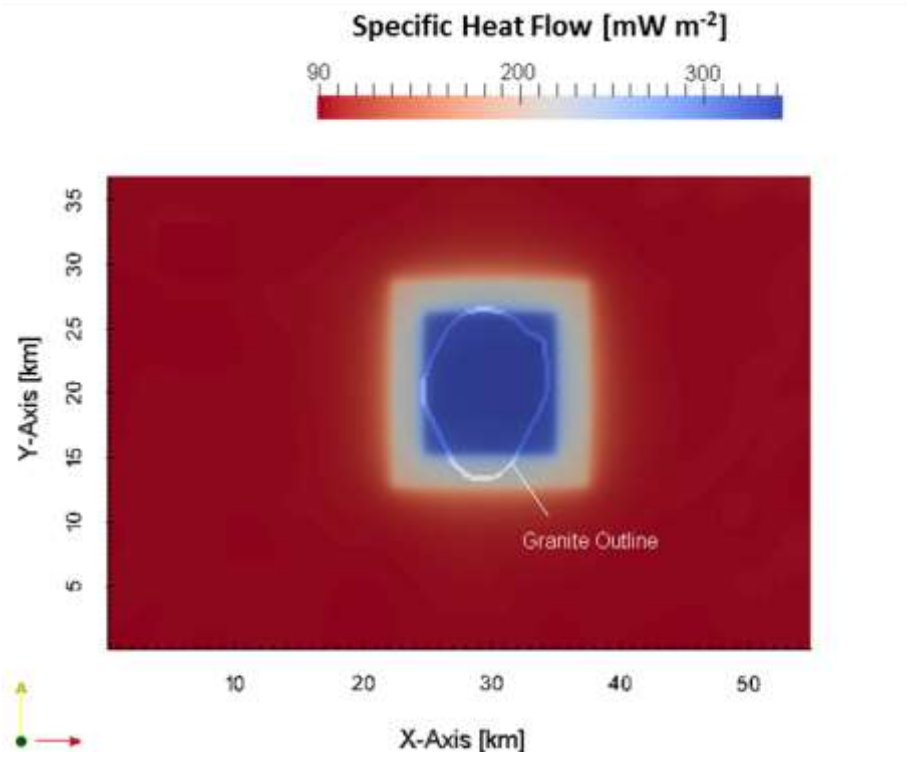

Figure 5: Basal specific heat flow distribution at the regional model base, heat flow in the order of 91 mW m^{-2} in the surrounding rocks and 360 mW m^{-2} at the base of the granite as obtained from regional conductive simulations

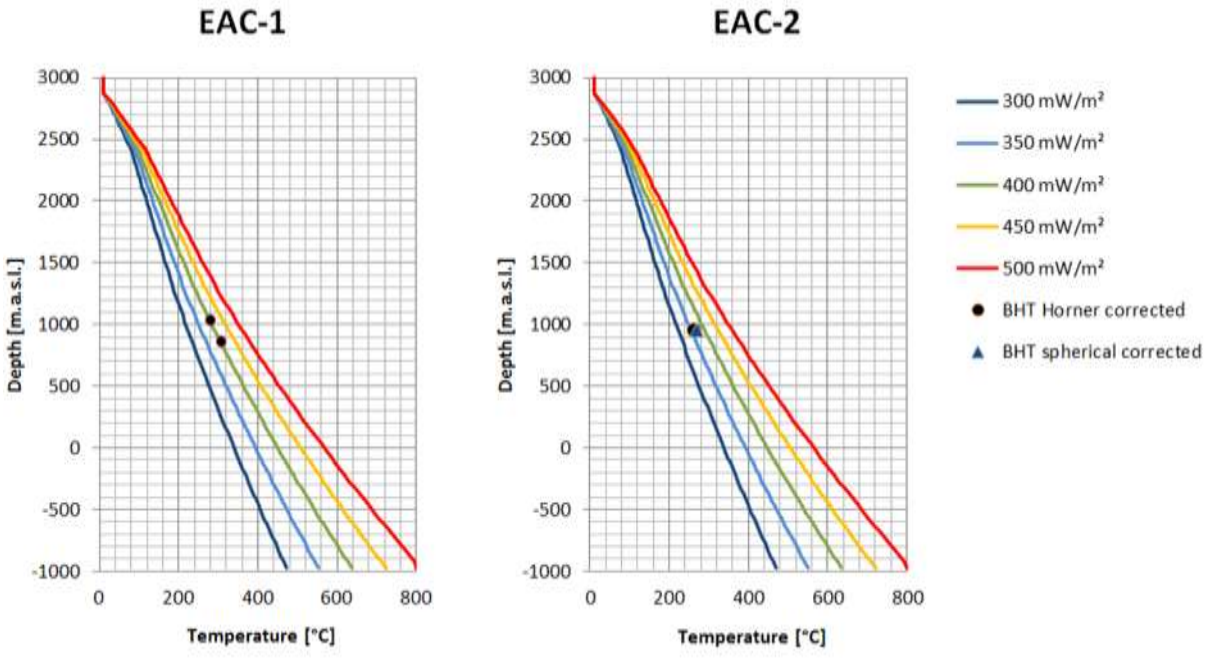

Figure 6: Temperature profile for well EAC-1 and EAC-2 obtained from conductive simulation with various specific heat flow conditions at the bottom, compared to stable BHT of the two wells

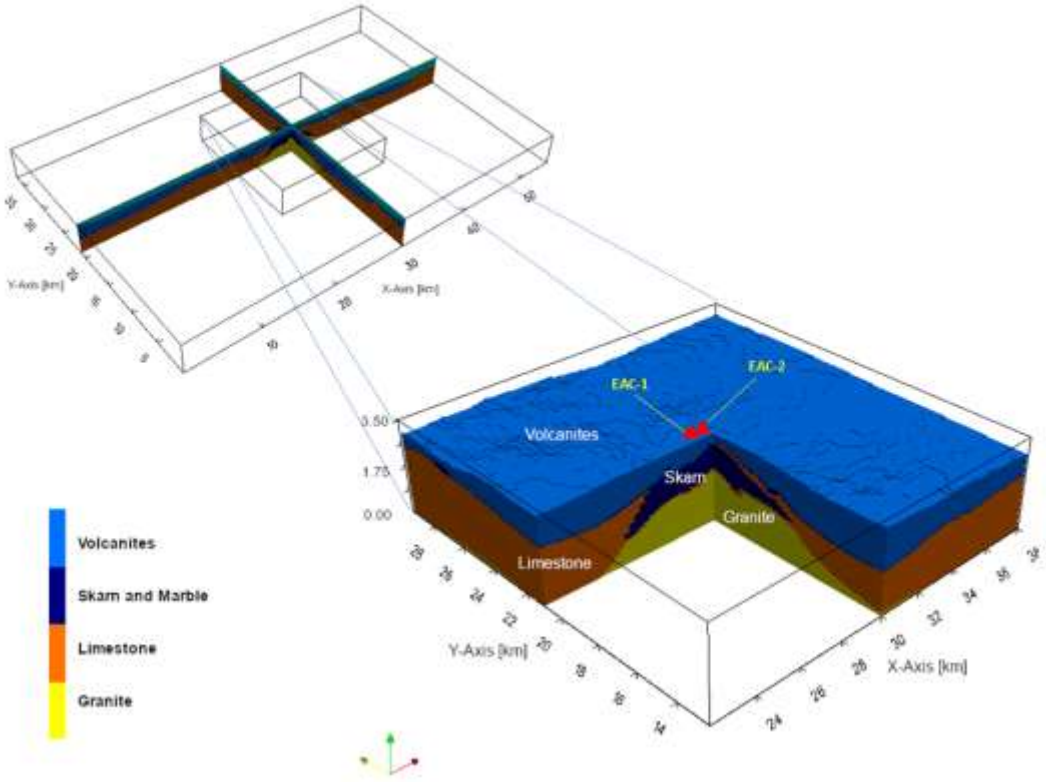

Figure 7: Regional model extent (top) and sliced local model for Monte Carlo simulations, different colours indicate the different modelled units and corresponds to the parametrised units in Table 3.

4.4 Stochastic Monte Carlo Simulations on local model

The available subsurface information limited to the two wells, EAC-1 and EAC-2 which are only about 500 metres away from each other imposes a huge uncertainty on 3D models which lacks information on spatial distribution of rock types. The modelled lithology based on these two wells do not necessarily reflect the geometry and heterogeneity of the Acoculco reservoir. In light of this limitation, we perform stochastic simulation to quantify the impact of uncertainties on input parameters in the final temperature prediction.

We cut out a small model from the regional model for detailed investigations. This local model has a dimension of 16 km × 17 km × 3.5 km and is extracted in a way that the granitic intrusion lies at the center (Figure 7). It comprises of the same lithological units as the regional model. The grid cells are equally discretised, holding a dimension of 150 m × 150 m × 50 m each, resulting in a total number of 846370 cells. The simulations are performed for heat transport by conduction only, as we expect no fluid flow in initial state.

To evaluate the impact of uncertainties of thermal conductivity and porosity on the formation temperature we perform steady state numerical Monte Carlo simulations with this local model. To this end, the physical properties such as thermal conductivity and porosity are treated as randomly distributed according to an observed or assumed distribution. We focus on the impact of uncertain thermal conductivity and porosity on the pre-production reservoir temperature at different target depths. Uncertainty is quantified in a Monte Carlo approach, using the algorithm of Sequential Gaussian Simulation (Deutsch and Journel, 1998) to generate a total number of 1500 realizations of the spatially varying thermal conductivity and porosity field.

We assigned a constant specific heat flow of 360 mW m^{-2} in the granite intrusion outline and 91 mW m^{-2} in the surrounding as Neumann boundary condition at the bottom of our domain. The top was fixed at a constant temperature of 12 °C implemented as Dirichlet boundary condition for the stochastic simulations. A test of a variation of the boundary conditions in a stochastic manner using a standard deviation of 25 % did not change the temperature field significantly. We therefore only varied thermal conductivity and porosity as single and combined parameters. Table 4 shows the used correlation lengths for the different rock types in three different scenarios.

4.4.1 Stochastic Parameters:

From the laboratory measurements, mean and standard deviations of matrix thermal conductivity and porosity were derived or compiled from literature (Table 3). Given these parameters a normal distribution was assumed to sample synthetically 1000 values per parameter as input for the Sequential Gaussian Simulation. For the granite lithology, in absence of lab data, the standard deviation is assumed to be 25 % from the mean. The used input distributions are shown in Figure 8.

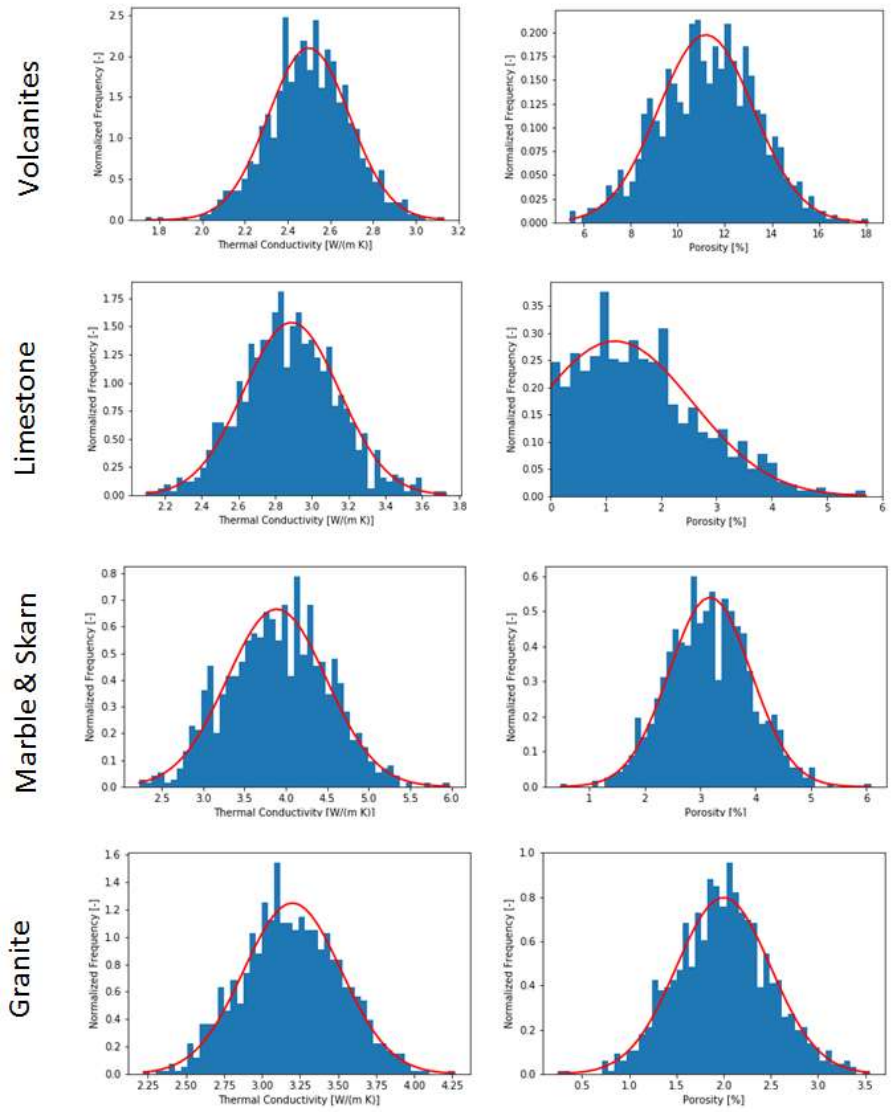

Figure 8: Rock property histograms used as input for SG Sim for the various rock types (left: thermal conductivity, right: porosity)

For a stochastic simulation, in addition to the variograms which defines the variability of a rock property, correlations lengths in each dimension has to be specified. From data collected from outcrop samples in Task 6.1, a spatial correlation length could not be determined due to strong impact of weathering and alteration on the rock samples. Therefore, we assumed three different correlation length scenarios and tested the sensitivity of the temperature field on these correlation lengths (Table 4). In most cases, we assumed a considerably shorter correlations length in vertical direction compared to the horizontal directions, which is motivated due to the fact that lithological units (beside the granitic intrusion) appear as layers.

Table 4: Assumed correlation lengths for different scenarios of stochastic simulations

Scenario	Unit	Correlation length [m]		
		x-direction	y-direction	z-direction
Basic Scenario 1	1: Volcanites	1500	1500	100
	2: Limestones	1500	1500	500
	3: Marble and skarn	500	500	500
	4: Granite	3000	3000	3000
Scenario 2	1: Volcanites	750	750	50
	2: Limestones	750	750	250
	3: Marble and skarn	250	250	250
	4: Granite	1500	1500	1500
Scenario 3	1: Volcanites	3000	300	200
	2: Limestones	3000	3000	1000
	3: Marble and skarn	1000	1000	1000
	4: Granite	6000	6000	6000

The basic scenario 1 assumes a horizontal correlation length of 1500 m in x- and y-direction and a correlation length of 100 m in z-direction for the volcanite unit. This represents the flow nature of the volcanic deposits, whose parameter distribution can be expected to change strongly between the different flow units in z-direction than laterally. For the limestones a horizontal correlation length of 1500 m and a vertical correlation length of 500 m is assigned, as we can expect the platform like deposits as well to change stronger in vertical than in lateral direction. More difficult is the assignment of a correlation length to the marble and skarn unit. The lithology is not deposited in a layer like structure, but is more dependent on the emplacement of specific dyke features. Therefore, we assume an isotropic correlation length of 500 m, implying smaller features with a local impact, rather than layer like structures. The granite intrusion is assumed to be the most homogeneous unit and the parameters have been distributed using a correlation length of 3000 m in all directions.

Scenario 2 and Scenario 3 were performed to test the sensitivity of the temperature field on the change of the correlation lengths. In order to evaluate this, the correlation lengths in all directions were halved (Scenario 2) and doubled (Scenario 3). The used correlation lengths in meters for each unit are listed in table 4.

Correlation lengths are assumed equally for thermal conductivity and porosity. For all simulations, a spherical variogram type without specific search angles has been used to distribute the parameters.

4.4.2 Results

The Monte Carlo ensemble mean provides a solid estimate of the temperature and its uncertainty (ensemble standard deviation) for the initial reservoir temperature (i. e. reservoir temperature under natural condition). Figure 9 shows the ensemble of realizations obtained by varying only thermal conductivity and only porosity stochastically at location of well EAC-1 for different correlation lengths. The realisations are compared to the bottom hole temperature (indicated by a red dot) of well EAC-1 and to the initial estimates of the possible range obtained from steady state simulations using only minimum value (mean – standard deviation) and maximum value (mean + standard deviation) of thermal conductivity and porosity in each layer (dashed lines). Figure 10 shows the ensemble of realisations for well EAC-1 where both thermal conductivity and porosity are varied at the same time.

From the results we can observe that the impact of uncertainties of thermal conductivity values (Figure 9, top row) on the temperature field is much more pronounced for all correlation lengths than the impact of porosity uncertainty (Figure 9, bottom row). This can be explained by the overall low porosity of the host rock, which results in very narrow range of the resulting bulk thermal conductivity.

From Figure 9, it can be observed that the reduction of uncertainty in temperature is strongly influenced by the correlation lengths. In general, increase in correlation length leads to a wider spread of the Monte Carlo ensembles at depth. This is because SGSim distributes the values randomly within the domain using the given correlation lengths. This implies that parameters at positions which are separated in distance by a length smaller than the correlations length vary only within the standard deviations. For the heat transport by conduction this implies that a large correlation length results in big features whose parameters are more equal, but as we perform a randomized distribution without a constraint, the position of the feature and the mean at the position are not fixed. This leads to wider spread observed in the temperature distributions. Smaller correlation lengths result in smaller features which are placed narrower in space and therefore lead to a more homogeneous distribution within the units. Another observation is the increase of uncertainty with depth, which can be observed for all correlation lengths and all parameters.

The stimulation for EGS system in Acoculco could be performed in two potential rock types – Skarn and Granite. We evaluate the results of these stochastic simulation runs quantitatively by comparing them at our expected stimulation depths. Table 5 presents the results of the simulation runs for temperature uncertainty at the top and bottom of skarn reservoir and granite reservoir. The mean ensemble temperatures with associated standard deviations for different correlation length (vertical columns) and different parameters (horizontal rows) is presented in the table.

In general, we find that the mean of the Monte Carlo ensemble does not change significantly with correlation lengths. The spread of the ensemble temperature profiles increases with larger correlation lengths. For a larger correlation length similar values of the properties (thermal conductivity and porosity) are assigned to a larger volume around the profile location (these values are slightly different in each realisation and lead to a wider spread. For shorter correlations lengths the values of the properties vary in a smaller volume in each realisation and the effect of different values cancels out.

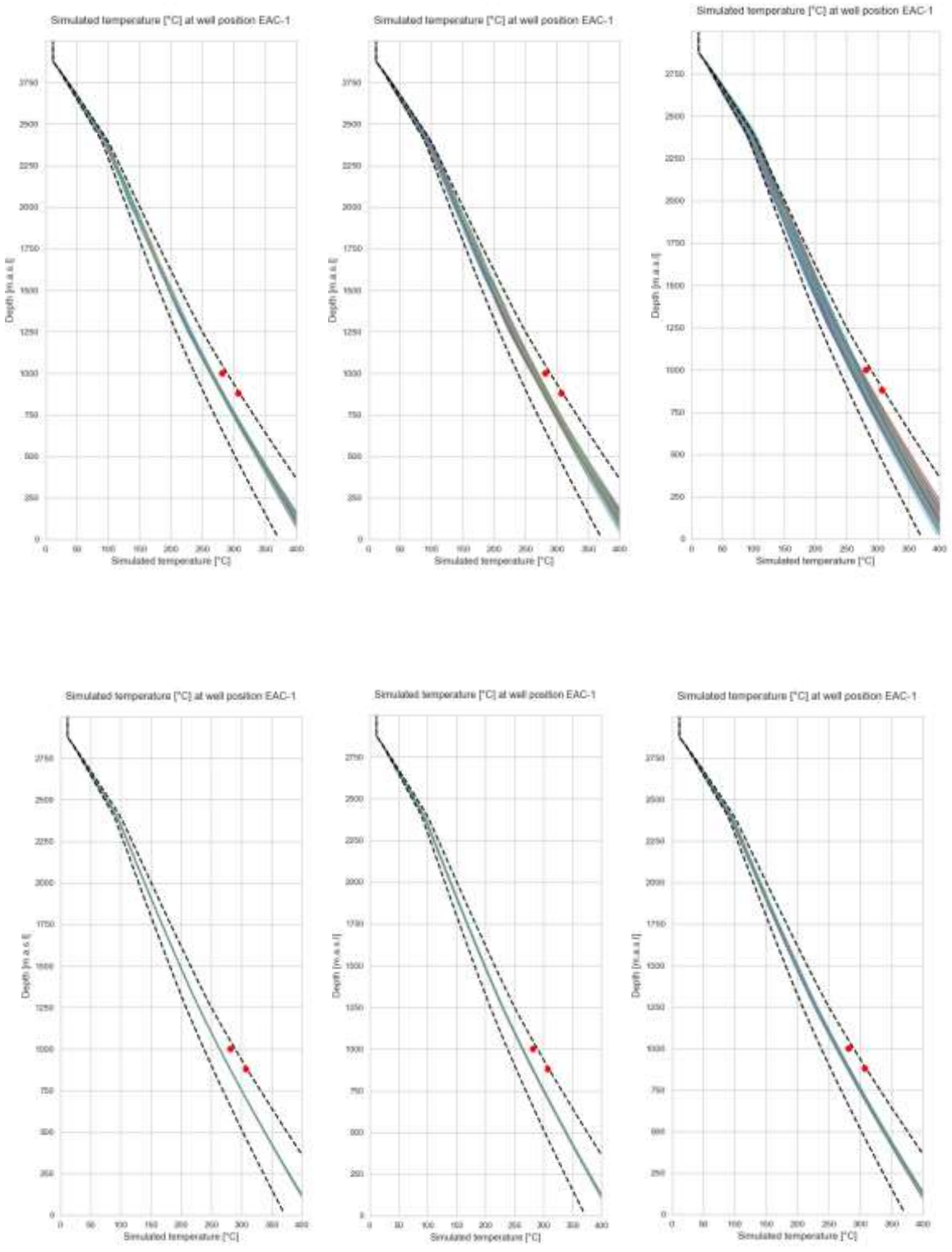

Figure 9: Simulated temperature profiles (colored lines) at the well positions of EAC-1 obtained from Monte Carlo simulation (with 1000 realisations) compared to the original uncertainty estimate (dashed lines) for increasing correlations (left-Scenario 2, middle –Scenario 1, right- Scenario 3). Stochastic distribution for thermal conductivity only (top row) and porosity only (bottom row). Red dots indicate Horner corrected temperatures at two different depths for well EAC-1

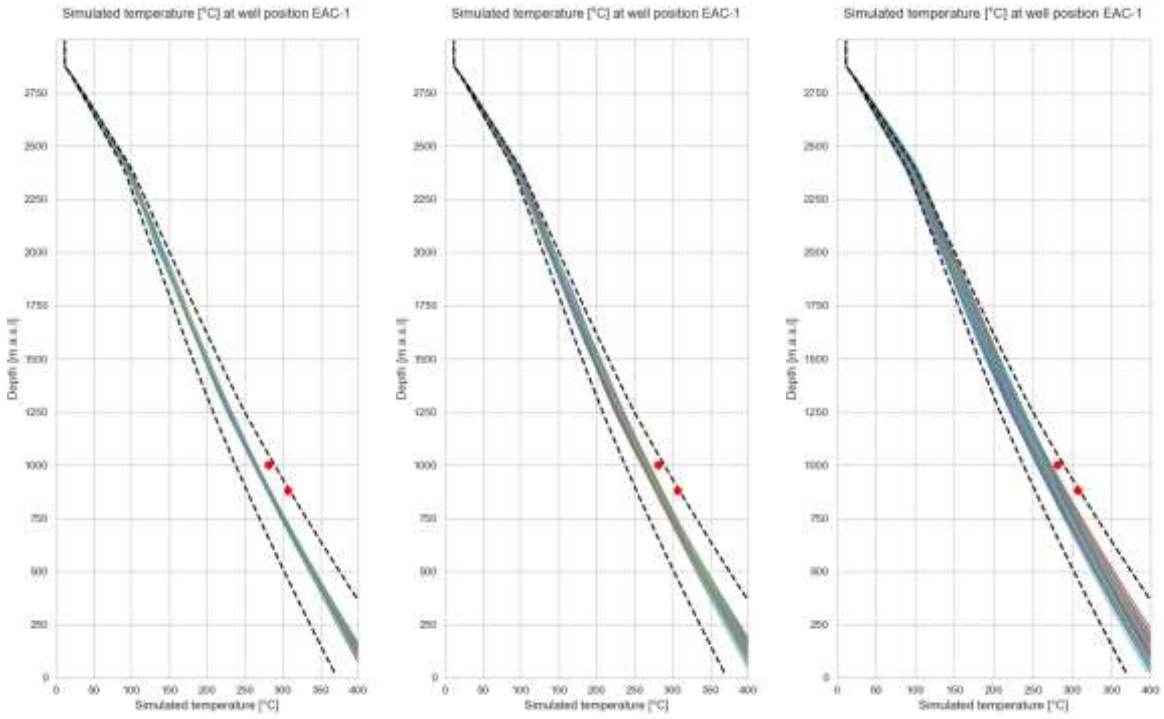

Figure 10: Simulated temperature profiles (colored lines) at the well positions of EAC-1 obtained from Monte Carlo simulation (with 1000 realisations) compared to the original uncertainty estimate (dashed lines) for increasing correlations (left-Scenario 2, middle –Scenario 1, right- Scenario 3). Stochastic distribution for both thermal conductivity and porosity only. Red dots indicate Horner corrected temperatures at two different depths for well EAC-1

In Figures 9 and 10, it can be observed that the initial estimates of uncertainty obtained from the two steady state simulations (with mean ± standard deviation of a property) indicated by the spread of the dashed lines reduces significantly when compared to the uncertainty indicated by the spread of realisations obtained from stochastic modelling.

For the granite reservoir model bottom (550 m.a.s.l.), the original uncertainty range in temperature estimated from the two envelope scenarios reduces from 71.01 K to 21.73 K for the longest correlation length. This corresponds to a reduction of the temperature range by 69 %. For the granite reservoir model top (1300 m.a.s.l.), the temperature ranges are reduced from 40.17 K to 15.46 K. This results in a decrease of temperature uncertainty in the order of 62 % compared to the envelope scenarios. Similar observations can be made for the Skarn reservoir (at 1650 m.a.s.l.) where the temperature uncertainty reduces from 30.28 K to 13.34 K resulting in a decrease of temperature uncertainty by 56 %.

Table 5 indicates that the mean of the Monte Carlo ensemble for the depths of interest does not change significantly for different modelled scenarios. We use the ensemble mean of the basic scenario (Scenario 1) as the best estimate for the temperatures at the model tops and bottoms. This results in a mean ensemble temperature of 332.10 °C for the bottom and 222.83 °C for the top of the reservoir established in the granite section and a mean temperature of 179.62 °C for the bottom and 91.25 °C for the top of the skarn reservoir scenario (Table 5). Using these formation temperatures for skarn and granite formations, we evaluate the potential of Acoculco as an EGS by simulating different production scenarios.

Table 5: Mean ensemble temperatures at expected stimulation depths obtained from stochastic simulation, the temperatures for specific depths are mean values of temperatures extracted at well positions EAC-1 and EAC-2

Stochastically distributed parameter	Position of evaluation	Scenario 2 (1/2 × basic correlation length)	Scenario 1 (basic correlation length)	Scenario 3 (2 × basic correlation length)
		Mean ensemble temperature [°C] (std. dev. [K]) (calculated from 500 realizations)		
Matrix thermal conductivity	Skarn reservoir top [2400 m.a.s.l.]	92.13 (1.00)	92.14 (1.60)	92.21 (2.36)
	Skarn reservoir bottom [1650 m.a.s.l.]	179.40 (1.10)	179.34 (1.90)	179.22 (3.01)
	Granite reservoir top [1300 m.a.s.l.]	221.67 (1.29)	221.55 (2.07)	221.41 (3.40)
	Granite reservoir bottom [550 m.a.s.l.]	330.64 (1.50)	330.58 (2.50)	330.41 (4.37)
Porosity	Skarn reservoir top [2400 m.a.s.l.]	91.29(0.23)	91.28 (0.44)	91.24 (0.74)
	Skarn reservoir bottom [1650 m.a.s.l.]	178.45 (0.18)	178.45 (0.42)	178.41 (0.82)
	Granite reservoir top [1300 m.a.s.l.]	221.05 (0.20)	221.02(0.41)	220.99 (0.84)
	Granite reservoir bottom [550 m.a.s.l.]	329.72 (0.27)	329.69(0.48)	329.64 (0.97)
Matrix thermal conductivity & porosity	Skarn reservoir top [2400 m.a.s.l.]	91.28 (0.78)	91.25 (1.26)	91.31(1.78)
	Skarn reservoir bottom [1650 m.a.s.l.]	179.74 (0.95)	179.62 (1.56)	179.49 (2.29)
	Granite reservoir top [1300 m.a.s.l.]	222.98 (1.10)	222.83 (1.70)	222.64 (2.71)
	Granite reservoir bottom [550 m.a.s.l.]	332.24 (1.20)	332.10 (2.17)	331.95 (3.18)

5 Evaluating the EGS potential in Acoculco

The technicalities of engineering permeability at depth is not within the scope of this study. We focus on evaluating the thermal effect on the field assuming the stimulation within the pre-existing wells EAC-1 and EAC-2 is successful. We consider that the two Acoculco wells which are approximately 500 m apart can be used as a geothermal doublet. We evaluate production from skarns and granites from a fracture zone formed by reactivating and connecting existing fractures and faults and establishing flow from the injection to the production well. Figure 11 shows a simplified schematic of the target stimulation zones.

5.1 Model geometry

From the stochastically parameterised local model, we extract reservoir volumes of 3.0 km × 2.0 km × 1.1 km comprising 134200 cells for two potential depth locations. The top and bottom of the reservoir volumes are extracted as such that it coincides with the top and bottom of the modelled skarn and granite units. Since the wells are very close to each other, the top and bottom of the modelled units do not differ in terms of elevation. The extent of the reservoir model is indicated by a red boundary in Figure 11. We perform transient simulations on these reservoir volumes. We evaluate the possibility of production from two target depths – one positioned within the skarn with a depth range from 2400 m.a.s.l. to 1650 m.a.s.l. while the other within the granite for a depth range from 1300 m.a.s.l. to 550 m.a.s.l., respectively. The stimulation midpoints in vertical direction for both wells are assumed to be at 1850 m.a.s.l. and at 1100 m.a.s.l. for Skarn and Granite respectively (Table 5). We rotate the model so that the fracture zone is aligned with the axis of the model and the permeability tensors are diagonal.

The extent of the stimulation zone depends strongly on the regionally and local stress patterns, mechanical properties of the rock, treatment parameters for stimulation (Hofmann et al., 2012, Reinicke 2009) and is limited to technical feasibility. To ensure numerical stability, the fracture zone is simulated as a three-dimensional rectangular volume instead of a 2D plane (Figure 12). The actual fracture aperture (of the order of mm) is many orders of magnitudes less than the numerical grid size (10 m). We consider a fracture zone of a width of 100 m and scale the permeability accordingly so that the resulting volumetric flow rate is the same as a single planar fracture. We refine the grid size of the extracted reservoir volume towards the well positions, to account for the higher fluid velocities near the producers and injectors (Figure 12). Grid dimensions in x- and y-directions are varying between 10 m and 142 m while the discretization in z-direction has been hold constant to 20 m. An example for the skarn reservoir is shown in Figure 12.

We assume the stimulated area to have its maximum horizontal extent of 1200 m per well in direction of the maximum horizontal stress SH_{max}. This horizontal extent should connect the two wells which are almost 550 m apart from each other. In Figure 12 left figure, the horizontal extent of the damage zone created due to stimulation is shown in yellow boundary while the right figure shows the vertical extent of the stimulation zone. Reinicke (2009) gives a range for vertical extent of fracture between 300 m to 1000 m depending on the stimulation technique. This is one of the most important factors as it determines the volume of the final stimulated reservoir. We investigate the impact of the vertical extent of the stimulation zone by simulating two different scenarios with fracture lengths of 100 m and 300 m respectively. Fracture length in our study is the vertical extent of the stimulated zone (Table 5).

We therefore simulate four reservoir volumes – two scenarios within skarn and two within granite, with two different vertical extents of the geothermal production volumes. These vertical extents are defined by

fracture length 300 m and 100 m. The top and bottom of the reservoir model with the top and the base of the possible stimulation scenarios are given in Table 6.

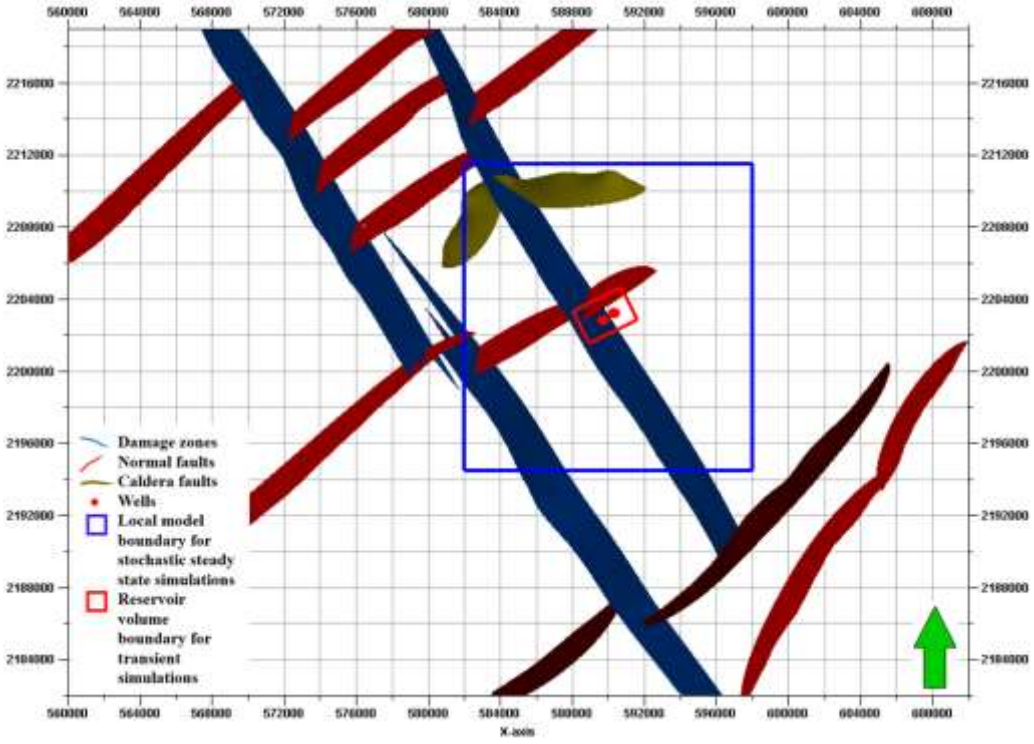

Figure 11: Model boundaries indicated in different colours, the outer boundary is the extent of the regional model, the main regional faults mapped within WP 3 and WP 4 are presented in figure, the inner blue boundary indicates the local model extent within which stochastic modelling is performed, the smallest red boundary within the model indicates the reservoir volume within which transient modelling is performed, EAC-1 and EAC-2 wells are indicated by two red dots

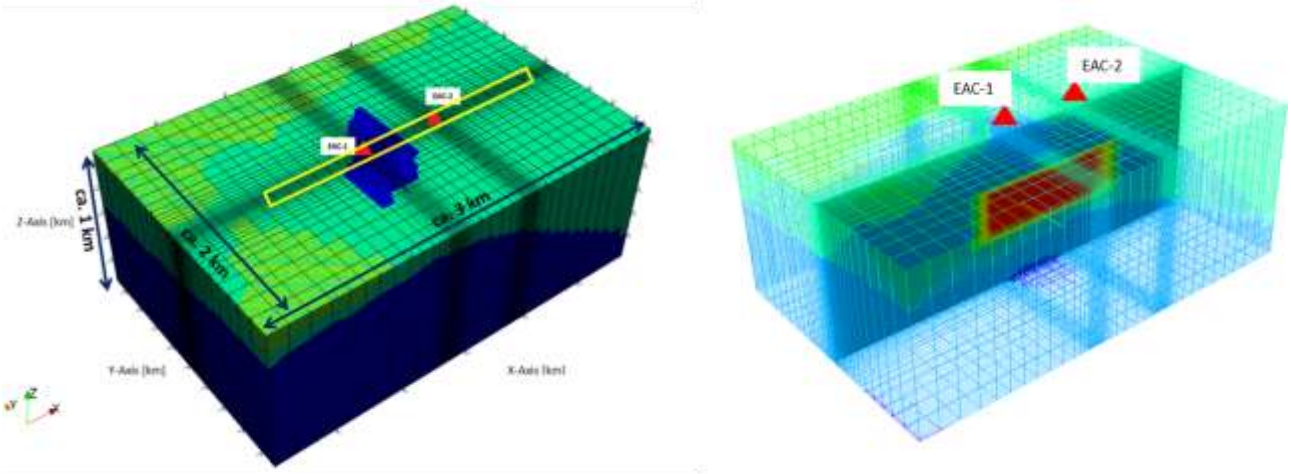

Figure 12: Gridding example for reservoir volumes, an example for Skarn reservoir is shown here, fine gridding approach towards the well location and coarser gridding away from the well (left), the central stimulated zone is modelled as a rectangular shaped zone indicated by the yellow boundary, the skarn is shown in blue color (modelled by WP 3), stimulation zone of 300 m vertical extent within the skarn reservoir volume is shown in the right figure.

Table 6: Depths in m.a.s.l. for reservoir volumes and stimulation zones within reservoir volumes

Reservoir Scenario	Model Base [m.a.s.l.]	Model Top [m.a.s.l.]	Stimulation Base [m.a.s.l.]	Stimulation Top [m.a.s.l.]	Stimulation Midpoint [m.a.s.l.]
Frac. length 300: Skarn	1650	2400	**1700**	**2000**	1850
Frac. length 100: Skarn	1650	2400	**1800**	**1900**	1850
Frac. length 300: Granite	550	1300	**950**	**1250**	1100
Frac. length 100: Granite	550	1300	**1050**	**1150**	1100

5.2 Hydraulic properties of the stimulation zone

We perform transient simulation by assuming hydraulic characteristics for the stimulation zones. Within the extracted reservoir model, we distribute permeability in a way that the central part of the stimulation zone has the highest permeability which decreases in steps towards the edges. We evaluate scenarios with two different permeability values applied to the central stimulated zone, 10^{-12} m² in and 10^{-13} m². As we move away from the central zone we decrease the permeability by one order of magnitude for the first 40 m, followed by a decrease by two order of magnitude in the next 20 m and finally reduced to 10^{-15} m² at the zone borders. Similar permeability values have been evaluated in other EGS systems. For example, in Soultz-Sous-Forêts (Vogt et al., 2012), the permeability range estimated is on the order of 10^{-12} m² to 10^{-14} m² (corresponding approximately to 1 darcy – 10 millidarcy) decreasing from the stimulation centre to the edges. Other studies show even lower permeability realized (Gholizadeh Doonechaly et al., 2013).

During testing of the reservoir scenarios, it turned out that a mean permeability lower than 10^{-13} m² for the stimulation zones leads to numerical instability due to the pressure drop between producer and injector. We therefore only simulate scenarios for a mean permeability of 10^{-12} m^2 and 10^{-13} m² in the central zone representing a more favourable stimulation result. The porosity of the stimulation zone is set constant to 2 %, increasing the host rock intrinsic porosity slightly, but not significantly.

The top and the bottom of the two reservoirs are assigned with a Dirichlet temperature boundary condition representing the ensemble mean temperature obtained from the stochastic simulations (Table 5). For the skarn reservoir a temperature of 91.25 °C was assigned to the top and a temperature of 179.62 °C to the bottom of the domain. The granite reservoir is at a deeper position and has a temperature of 222.83 °C at the top of the model domain and 332.10 °C at the base respectively. Prior to the production scenarios, an undisturbed temperature field for the reservoir models is obtained by running a steady-state simulation.

In the doublet configuration, EAC-1 is used as the injector and EAC-2 as producer. We assume three cells for production and injection implying a liner or open-hole interval of 60 m in total for fluid inflow into the well.

All the simulations are tested with three circulation rates, 10 Ls^{-1}, 30 Ls^{-1} and 50 Ls^{-1} (constant over time). This range covers the lower end of flow rates established in operating EGS reservoirs (e. g. Vogt et al., 2012) as well as the economically favourable flow rate (50 Ls^{-1}). The injection temperature is chosen to 70 °C to

inhibit mineral precipitation and clogging of the injection wells (Li and Lior, 2014). For all simulations we assume 100 % water recovery and no loss to the formation. As SHEMAT-Suite allows only a volume input and volume extraction of water at the injector and the producer cells, the fluid properties of the extracted and injected water (density, specific heat capacity and fluid dynamic viscosity) are set constant adjusted to the mean reservoir temperature. Variable fluid properties with temperature lead to a pressure increase within the system due to the imbalanced mass injection and extraction of constant volumes at different fluid densities. This effect is avoided by fixing the fluid properties to a constant value. The model properties are listed in Table 7.

Table 7: Model properties for transient simulations on reservoir volumes

	Skarn Reservoir Value	**Granite Reservoir Value**
Model size	$3000 \times 2000 \times 1100$ m^3	$3000 \times 2000 \times 1100$ m^3
Mesh size	$61 \times 40 \times 55$ m^3	$61 \times 40 \times 55$ m^3
Resolution	x: 10 m – 142 m y: 10 m – 135 m z: 20 m	x: 10 m – 142 m y: 10 m – 135 m z: 20 m
Stimulated volumes	$1150 \times 100 \times 100$ m^3 $1150 \times 100 \times 300$ m^3	$1150 \times 100 \times 100$ m^3 $1150 \times 100 \times 300$ m^3
Temperature at top	91.25 °C	222.83 °C
Temperature at bottom	179.62 °C	332.10 °C
Simulation time	30 Years	30 Years
Permeability	10^{-12} m², 10^{-13} m²	10^{-12} m², 10^{-13} m²
Circulation rate	10 Ls^{-1}, 30 Ls^{-1}, 50 Ls^{-1}	10 Ls^{-1}, 30 Ls^{-1}, 50 Ls^{-1}
Temperature of injected water	70 °C (EAC-1)	70 °C (EAC-1)
Constant fluid dynamic viscosity*	2.06×10^{-4} Pa s (@ 135 °C)	9.58×10^{-5} Pa s (@ 283 °C)
Constant fluid density*	935.59 kg m^{-3} (@ 135 °C)	761.93 kg m^{-3} (@ 283 °C)
Constant fluid specific heat capacity*	4248 J kg^{-1} K^{-1} (@ 135 °C)	5079 J k^{-1} K^{-1} (@ 283 °C)
Constant fluid thermal conductivity*	0.69 W m^{-1}K^{-1} (@ 135 °C)	0.59 W m^{-1}K^{-1} (@ 283 °C)

*constant values for fluid properties for a salinity of 0 mg L^{-1} at reservoir pressure assumed to balance mass injection and extraction (IAPWS-IF97).

5.3 Results

In the following section we present the simulation results to test the sensitivity of production temperature and pressure over time for the two target rock types - skarn and granite, two fracture lengths – 100 m and 300 m representing two different fracture volumes and two different permeability values – 10^{-12} m^2 and 10^{-13} m^2.

5.3.1 Stimulation in Skarn

The results of the simulations for production from skarn reservoir for two different fracture lengths are shown in Figure 14 and 15. The temperature and the thermal power evolution over 30 years of production for three different circulation rates and two different mean permeabilities of the inner stimulation zone are shown. It should be noted, that the temperature and pressure estimates are evaluated at the bottom hole of the wells, this implies that cooling of the fluid in the ascending process within the well is neglected. The results can be summarised in the following main points:

- For the smaller reservoir extent (Figure 13, left), the temperature decreases much faster leading to thermal breakthrough already within the first few years of production. Even for the model with the larger stimulation volume (Figure 13, right) and economically reasonable conditions for a retrieved water volume of 30 L s^{-1} to 50 Ls^{-1}, the thermal breakthrough occurs within the first 10 years.

- For a very low flow rate 10 Ls^{-1} within a larger stimulated volume, the thermal breakthrough occurs much later. This effect can be explained by the decreased Darcy velocity in the larger volume and therefore longer time window for the fluid to heat up. However the corresponding thermal power generated is also very low questioning the economic feasibility of this flow rate.

- The influence of permeability is small and even negligible for the greater reservoir volume (fracture length = 300 m, Figure 13 right) as compared to the smaller reservoir volume (Figure 13 left).

- Thermal power calculated using Equation 7 (which scales linearly with flow rate and temperature difference between injector and producer) is high for high flow rates in the first years but decreases rapidly after due to the constant injection temperature of 70 °C and the decreasing temperature difference ΔT between producer and injector over the whole production cycle.

- Although higher temperatures are achieved for the low permeability scenarios, the pressure evolution at the producer (Figure 16) and the resulting reservoir impedance (Table 8), favour a higher permeability for a sustainable production. The pressure built up reflects strongly the restricted volume of the small reservoir model.

- To ensure commercial feasibility of any reservoir, the reservoir impedance (calculated using Equation 10) should not exceed 100 kPa s L^{-1} (Clauser, 2006). For the two 10^{-12} m² permeability scenarios, the reservoir impedance lies within the feasible range for both geometries (Table 8). However for the low permeability scenario of 10^{-13} m², it exceeds beyond the 100 kPa s L^{-1} threshold indicating least feasible scenario for economic production.

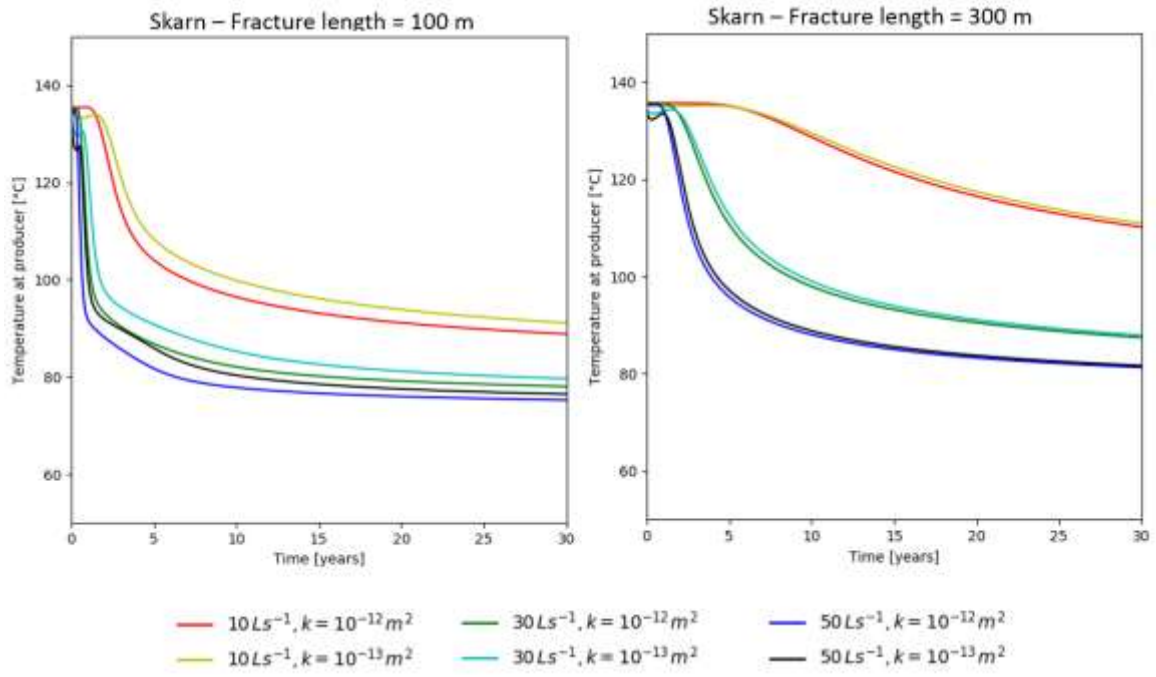

Figure 13: Temperature vs time for production from Skarn for different flow rates, permeability and fracture lengths

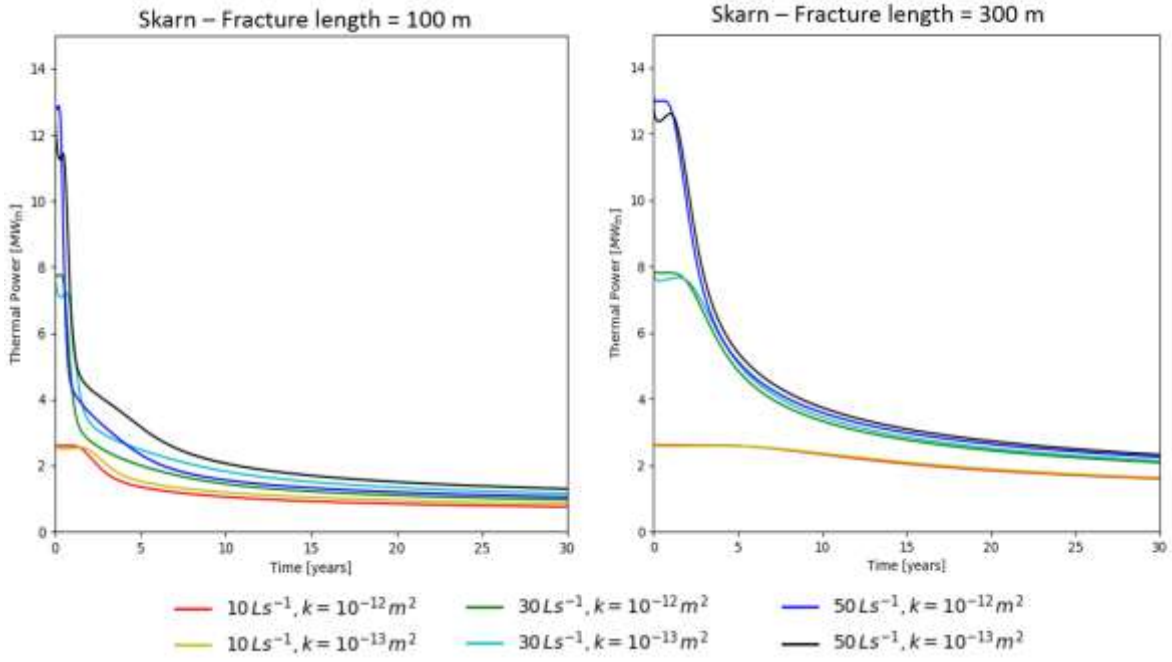

Figure 14: Thermal power vs time for production from Skarn for different flow rates, permeability and fracture lengths

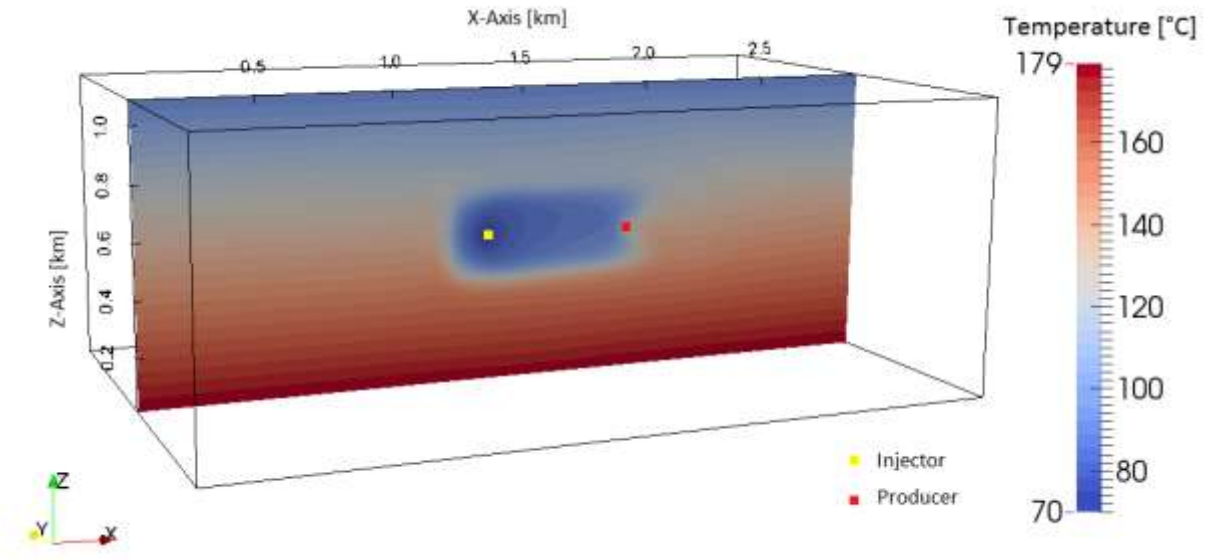

Figure 15: Temperature distribution within the larger skarn reservoir after 30 years of production in the low permeability scenario of 10^{-13} m² for a circulation rate of 30 L s^{-1}, the injector and producer stimulation points are indicated by yellow and red respectively.

Figure 15 shows a cross-section with the temperature distribution after 30 years of production for permeability 10^{-13} m^2 and for a circulation rate 30 Ls^{-1}. It can be observed that with a flow rate of 30 Ls^{-1}, thermal breakthrough is reached within 5 years. However sustainable production is ensured with flow rates in the order of 10 Ls^{-1}.

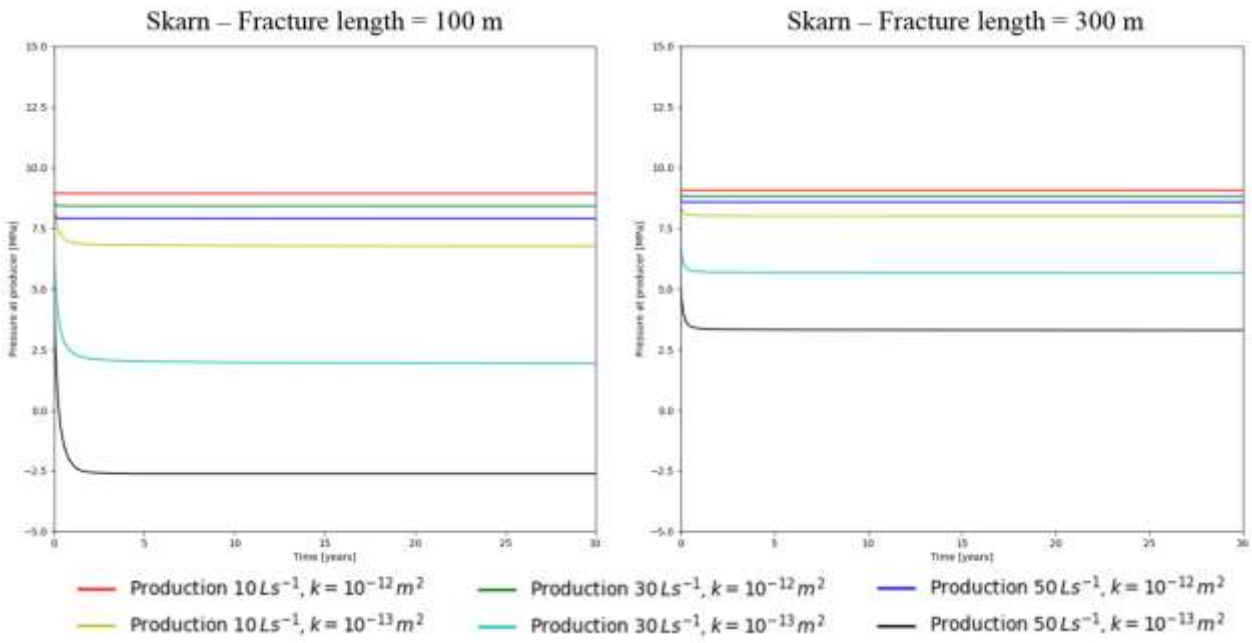

Figure 16: Pressure vs time for producer at different flow rates and permeability values for Skarn reservoir

Table 8: Reservoir Impedance for different simulated volumes and permeability in Skarn

Reservoir scenario	Permeability [m^2]	Circulation rate [Ls^{-1}]	Reservoir Impedance [kPa s L^{-1}]
Skarn small reservoir Scenario 1	10^{-12}	10/ 30/ 50	57.71/ 57.90/ 58.19
Skarn small reservoir Scenario 1	10^{-13}	10/ 30/ 50	532.67/ 535.91/ 533.33
Skarn large reservoir Scenario 2	10^{-12}	10/ 30/ 50	25.38/ 25.42/ 25.50
Skarn large reservoir Scenario 2	10^{-13}	10/ 30/ 50	248.33/ 249.10/ 249.95

5.3.2 Stimulation in granite:

The results of the simulations for the two granite reservoir scenarios comprising the different stimulated volumes are shown in Figure 17 and 18. The temperature and the thermal power evolution over 30 years of production looks very similar to the results for the skarn reservoir. The main observations can be summarised as follows:

- In the small reservoir volume (Figure 17, left), temperature decreases much faster leading to thermal breakthrough as well within the first few years of production. In the larger reservoir volume, temperature stabilizes at a higher level of 120 °C for the 50 Ls^{-1} circulation rate which can be still at economically reasonable level (Figure 17, right).

- Higher permeability of the stimulation zone leads within the granite as well to a lower temperatures after 30 years of production.

- The hypothetical thermal power output correlates with the production temperature drop, as seen within the skarns, but stabilizes after a string drop at around 2.5 MW_{th} for the small reservoir scenario after almost 3 years of production. It is interesting to note that the thermal power output for the smaller reservoir extent differs negligibly for different permeability values or circulation rates.

- For the larger reservoir extent, however the thermal power output stabilises between 7 MW_{th} to 10 MW_{th}, depending on circulation rates.

- The pressure evolution at the producer (Figure 19) and the resulting reservoir impedance (Table 9) for the larger reservoir extent is favourable for both permeability scenarios for a sustainable production.

- Reservoir impedance for the low permeability scenario of 10^{-13} m^2 exceeds only for the small reservoir models beyond the 100 kPa sL^{-1} threshold (Table 9). Commercial feasibility can therefore not be ensured for this scenario, whereas the other scenarios could be feasible in terms of the pressure established.

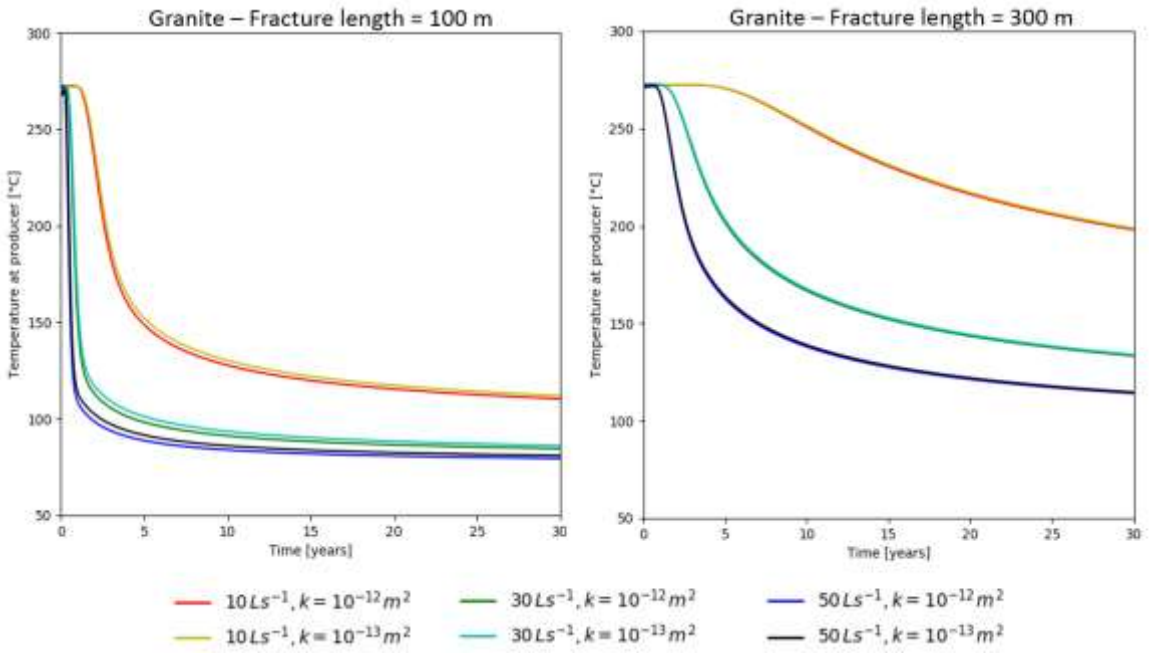

Figure 17: Temperature vs time for 30 years for production from Granite reservoir volume for different flow rates, permeability and fracture lengths

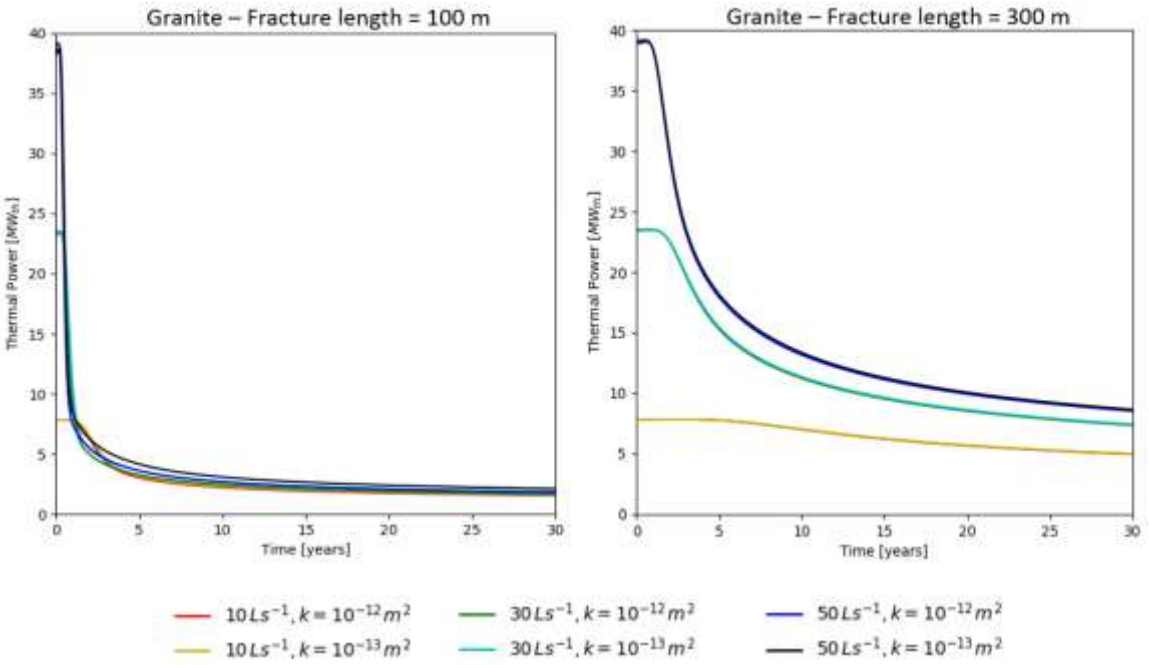

Figure 18: Thermal power vs time for 30 years for production from Granite reservoir volume for different flow rates, permeability and fracture lengths

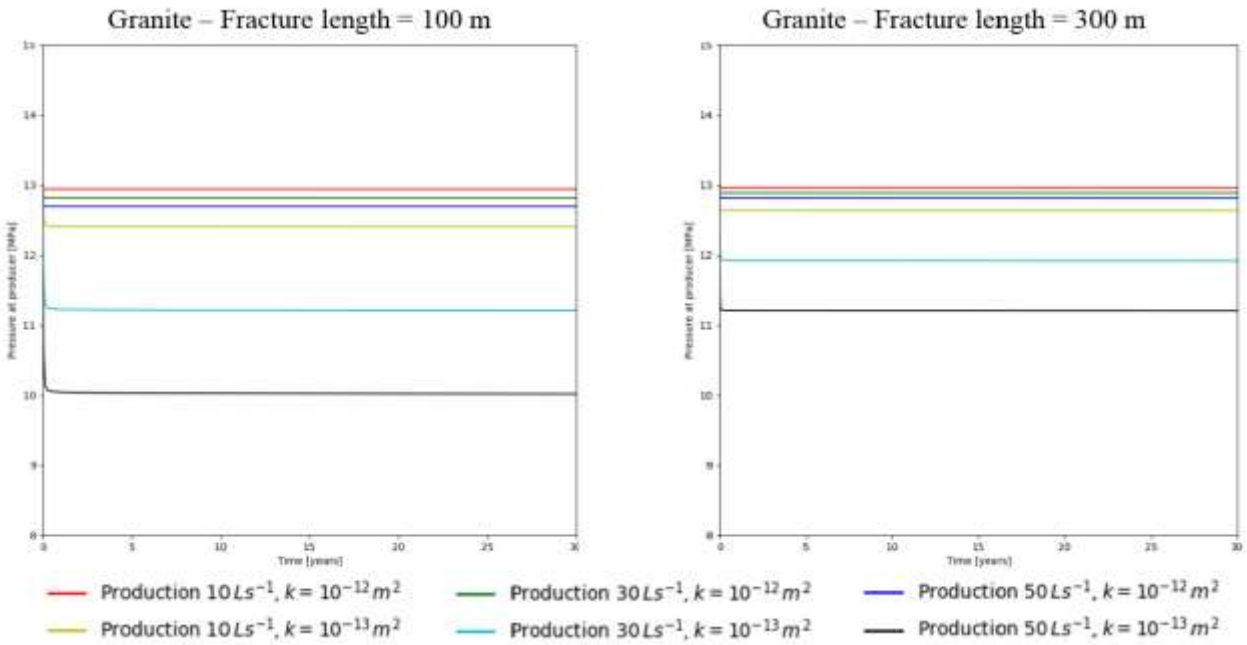

Figure 19: Pressure vs time for producer at different flow rates and permeability values for Granite reservoir

Table 9: Reservoir Impedance for different simulated volume and permeability in granite

Reservoir scenario	**Permeability [m²]**	**Circulation rate [Ls^{-1}]**	**Reservoir Impedance [kPa s L^{-1}]**
Granite small reservoir Scenario 1	10^{-12}	10/ 30/ 50	13.29/ 13.32/ 13.32
Granite small reservoir Scenario 1	10^{-13}	10/ 30/ 50	130.48/ 130.86/ 130.87
Granite large reservoir Scenario 2	10^{-12}	10/ 30/ 50	7.43/ 7.43/ 7.43
Granite large reservoir Scenario 2	10^{-13}	10/ 30/ 50	74.01/ 74.08/ 74.08

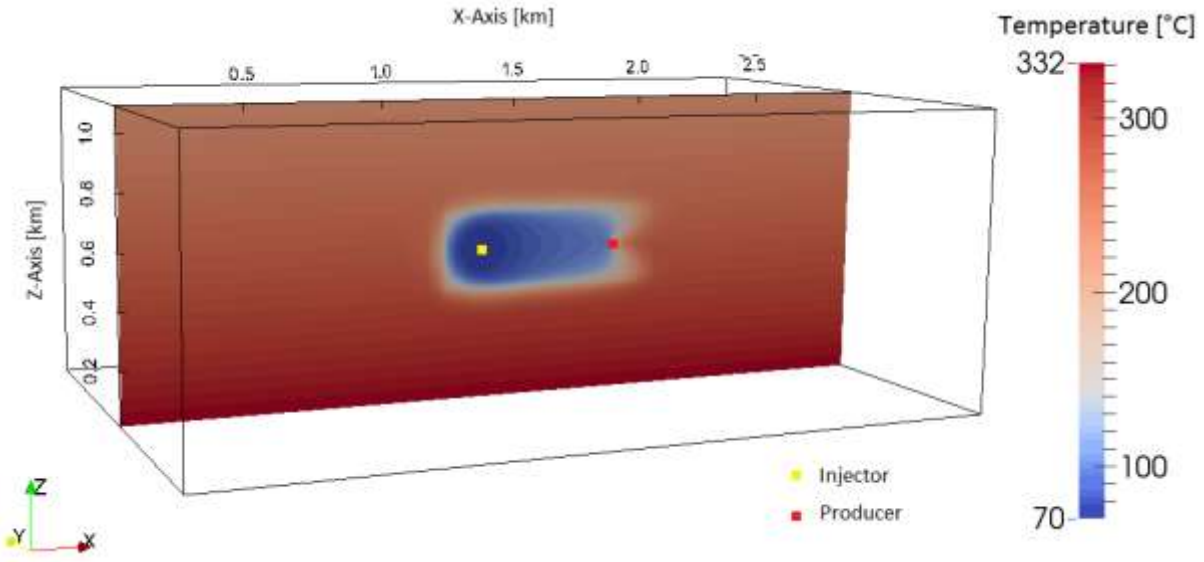

Figure 20: Temperature distribution after 30 years of operation within the larger granite reservoir for a production rate of 30 Ls^{-1} and the lower permeability of 10^{-13} m^2, the yellow dot and the red dot indicates the injection point and production point respectively.

Figure 20 shows a vertical section with stimulation points of well EAC-1 and EAC-2 indicated by the yellow and red dots respectively. After 30 years of production with a flow rate of 30 Ls^{-1}, the temperature stabilises at around 120 °C.

It is important to note that the viscosity differences of the fluid at the producer and injector have a strong influence on the pressure. Our scenarios, assuming constant fluid properties reflect the most favourable case of a low viscosity at the injector. Due to the symmetrical geometry of the reservoir models and the well positions, pressure built up and drop down are symmetrical to the initial pressure. In a real case, pressure drop down and built up would not establish symmetrically, due to different fluid densities and dynamic viscosities as a result of the temperature difference. For our reservoir model, coupling of fluid properties to temperature leads to an imbalance of mass and a pressure built up throughout the whole reservoir, due to the restriction of flow rate input as volumes, rather than mass.

6 Conclusion

Our work represents an initial overview of a possible EGS in Acoculco based on several assumptions. We presented scenarios based on assumptions of realizable permeability in the order of 10^{-12} m^2 and 10^{-13} m^2 and initial estimates of producible geothermal volumes (stimulated volume connecting the two well) in the order of 0.005 km^3 and 0.02 km^3. However we recognize that the assumptions of these producible stimulated volumes are probably very low for commercial purposes. In addition, the range of assumed permeability is highly optimistic. The production scenarios within our stimulated reservoir volumes for a permeability lower than 10^{-13} m^2 failed due to numerical instability.

The results however lead to some important conclusions:

- The main factors influencing the temperature distribution during production are the flow rates and the stimulated volumes. It is clear that in order to have a commercial production, larger fracture volumes need to be achieved so that the injected water has sufficient time to get heated up.

- From the temperature point of view, the depth of stimulation in granite reservoir with 300 m vertical fracture extent is more favorable. If stimulation is successful within this depth range, the temperature estimated over 30 years of production stabilizes at around 130 °C for circulation rates of 50 Ls^{-1} and the hypothetical thermal power output is much larger (~ 11 MW_{th}) than within the shallow skarn target.

- Due to the local stress field and fault networks, it it is not clear to what extent a pre-existing fracture network can be reactivated by a hydraulic stimulation at Acoculco. A connection to these fault features is not considered in our simulations, due to the distance and the technically feasible horizontal stimulation extent.

- A connection to a higher permeability zone of larger extent could as well optimize the pressure built up and drop between the wells and allow for efficient mixture and heat up of the injected fluids.

- In further work, the stimulation design and the mechanical impact influencing the fracture propagation and directions have to be evaluated carefully to provide better insights into the amount of stimulated volume and its transmissivity and permeability.

- Mechanical sealing effects due to mineral precipitation, reducing permeability and porosity with time should be investigated as they may lead to mechanical clogging and flow path way alteration (Pape et al., 2005).

- A connection to a higher permeability zone of larger extent could as well optimize the pressure built up and drop between the wells and allow for efficient mixture and heat up of the injected fluids.

7 Acknowledgement:

We thank the Comision Federal di Electricidad (CFE) for providing data and information regarding their geothermal wells and the entire GEMex consortium comprising of Mexican and European partners for the cooperation and unpublished inputs on conceptual ideas which are used for this study.

Laboratory measurements used in this study are performed in Task 6.1 within WP 6 and we would like to thank all Task 6.1 partners (TUDA, UNITO, GFZ, BGS) who contributed to the field work, sample collection, measurements and data analysis.

8 References

Avellán, D.R., Macías, J.L., Layer, P. W., Cisneros, G., Sánchez - Núñez, J.M., Gómez-Vasconcelos, Pola, A., Sosa-Ceballos, G., García-Tenorio, F., Reyes-Agustín, G., Osorio-Ocampo, S., García-Sánchez, L., Mendiola, F., Marti, J., López-Loera, H., and Benowitz, J, 2018, Geology of the Late Pliocene – Pleistocene Acoculco caldera complex, eastern Trans-Mexican Volcanic Belt (México), *Journal of Maps*, https://doi.org/10.1080/17445647.2018.1531075.

Calcagno, P., Evanno, g., Trumpy, E., Gutiérrez-Negrín, L. C., Macías, J. L., Carrasco-Núñez, G., Liotta, D., 2018. Preliminary 3-D geological models of Los Humeros and Acoculco geothermal fields (Mexico) – H2020 GEMex Project., *Advances in Geosciences, 45,* 321 – 333.

Canet, C., Hernández-Cruz, B., Jiménez-Franco, A., Pi, T., Puláez, B., Villanueva-Estrada, R. E., Alfonso, P., González-Partida, E., 2015. Combining ammonium mapping and short-wave infrared (SWIR) reflectance spectroscopy to constrain a model of hydrothermal alteration for the Acoculco geothermal zone, Eastern Mexico, *Geothermics, 53,* 154-165.

Carrasco-Núñez, G., López-Martínez, M., Hernández, J., Vargas, V., 2017. Subsurface stratigraphy and its correlation with the surficial geology at Los Humeros geothermal field, eastern Trans-Mexican Volcanic Belt, Geothermics, 67, 1 – 17.

Clauser, C., 1984. A climatic correction on temperature gradients using surface temperature series of various periods. *Tectonophysics, 103,* 33 – 46.

Clauser, C., 2006. Geothermal energy. In: Heinloth, K., (ed.). Landolt-Börnstein, Group VIII: Advanced Material and Technologies, Vol. 3: Energy Technologies, Subvol. C: Renewable Energies. Springer Verlag, Heidelberg-Berlin.

Davies, J. H., 2013. Global map of solid Earth surface heat flow. *Geochem. Geophys. Geosyst., 14,* 4608 – 4622.

Deutsch, C. V., Journel, A. G., 1998. GSLIB. Geostatistical software library and user's guide, University Press, Oxford.

García-Palomo, A., Macías, J. L., Tolson, G., Valdez, G., Mora, J. C., 2002. Volcanic stratigraphy and geological evolution of the Apan region, east central sector of the Trans-Mexican Volcanic Belt. G*eofísica Internacional, 41(2),* 133 – 150.

García-Tovar, G. P., Martínez-Serrano, R. G., Solé, J., Correa-Tello, J. C., Nuñez-Castillo, E.Y., Guilluo, J., Monroy-Rodríguez, E., 2015. Geología, geocronología y geoquímica del vulconismo Plio-Cuaternario del Campo Volcánico Apan-Tecocomulco, *Faja Volcánica Trans-Mexicana. Rev. Mex. Cienc. Geol., 32 (1),* 100-122.

Gholizadeh Doonechaly, N., Rahman, S.S., Kotousov, A., 2013. A New Approach to Hydraulic Stimulation of Geothermal Reservoirs by Roughness Induced Fracture Opening, In Jeffrey, B. (ed.), *Effective and Sustainable Hydraulic Fracturing,* Commonwealth Scientific and Industrial Research Organisation, Australia, doi:10.5772/45724.

Hofmann, H., Babadagli, T., Zimmermann, G., 2012. Hydraulic Fracturing Scenarios for Low Temperature EGS Heat Generation from the Precambrian Basement in North Alberta, *GRC Transactions, 36*, 459 – 468.

Kolditz, O., Clauser, C., 1998. Numerical simulation of flow and heat transfer in fractured crystalline rocks: application to the hot dry rock site in Rosemanowes (U.K.), *Geothermics, 27(1),* 1-23.

Li, Mengying., Lior, Noam., 2014. Comparative analysis of powerplant options for Enhanced geothermal Systems (EGS). *Energies*, 7, 8427 – 8445, doi: 10.3390/en7128427

López-Hernándes, A., García-Estrada, G., Aguirre-Díaz, G., González-Partida, E., Palma-Guzmán, H., Quijano-Léon, J. L., 2009. Hydrothermal activity in the Tulancingo-Acoculco Caldera Complex, central Mexico: Exploratory studies. *Geothermics, 38,* 279 – 293.

Lorenzo Pulido, C., Flores Armenta, M., Ramírez Silva, G., 2010. Characterization of the Acoculco Geothermal Zone as HDR System. *GRC Transactions, 34 (2010).*

Macías, J.L., Arce, J.L., García-Tenorio, F., Layer, P.W., Rueda, H., Reyes-Augustin, G., Avellán, D., 2012. Geology and Geochronology of Tlaloc, Telapón, Iztaccíhuatl, and Popocatéplet Volcanoes, Sierra Nevada, Central México, *GSA Field Guides, 25,* 163 – 193.

MIT, 2006. The future of geothermal energy: impact of enhanced geothermal systems (EGS) on the United States in the 21st century. *Report MIT - Massachusetts Institute of Technology, Cambridge, Massachusetts.* Available online: https://www1.eere.energy.gov/geothermal/pdfs/future_geo_energy.pdf

Pape, H., Clauser, C., Iffland, J., Krug, R., Wagner, R., 2005. Anhydrite cementation and compaction in geothermal resrvoirs: Interaction of pore-space structure with flow, transport, p-t-conditions, and chemical reactions, *International Journal of Rock Mechanics and Mining Science, 42,* 1056 – 1069.

Pardó M., Suárez, G., 1995. Shape of the subducted Rivera and Cocos plates in southern Mexico: Seismic and tectonic implications. *Journal of Geophysical Research, 100(B7),* 12357 – 12373: *doi:10.1029/95JB00919.*

Peaceman, D.W., 1983. Interpretation of well-block pressure in numerical reservoir simulation with non-square grid blocks and anisotropic permeability, *Society of Petroleum Engineers Journal, 23(3),* 531-543.

Pollack, H. N., Hurter, S. J., Johnson, J., R., 2010. Heat flow from the earth's interior: Analysis of the global data set. *Review of Geophysics, 31,* 267-280.

Reinicke, A., 2009. Mechanical and Hydraulic Aspects of Rock-Proppant Systems: Laboratory Experiments and Modelling Approaches, *Doctoral Dissertation*, University of Potsdam, Potsdam, Germany.

Roure, F., Alzaga-Ruiz, H., Callot, J.-P., Ferket, H., Granjeon, D., Gonzalez-Mercado, G. E., Guilhaumou, N., Lopez, M., Mougin, P., Ortuno-Arzate, S., Séranne, M., 2009. Long lasting interactions between tectonic loading, unroofing, post-rift thermal subsidence and sedimentary transfers along the western margin of the Gulf of Mexico: Some insights from integrated quantitative studies, *Tectonophysics, 475,* 169 – 189.

Rybach, L., 1976. Radioactive Heat Production: A Physical Property Determined by the Chemistry of Rocks, In: Strens, R. G. J. (ed.), *The Physics and Chemistry of Minerals and Rocks*, 309 – 318, Wiley & Sons, London

Rybach, L., 1986. Amount and Significance of Radioactive Heat Sources in Sediments, In: Burrus, J. (ed.), *Thermal Modelling in Sedimentary Basins, Editions Technip*, 311-322., France

Schön, J. H., 2004. *Physical Properties of Rocks: Fundamentals and Principles of Petrophysics*, 1. Edition, Elsevier, Amsterdam.

Smerdon, J. E., und Stieglitz, M.,2006. Simulating heat transport of harmonic temperature signals in the Earth's shallow subsurface: Lower boundary of sensitivities, *Geophys. Res. Lett., 33,* L14402, doi: 10.1029/2006GL026816.

Sosa-Ceballos. G., Macías, J.L., Avellán, D.R., Salazar-Hermenegildo N., Boijseauneau-López, M.E., Pérez-Orozco, J.D., 2018. The Acoculco Caldera Complex magmas: Genesis, evolution and relation with the Acoculco geothermal system, *Journal of Volcanology and Geothermal Reserarch, 358,* 288-306.

Suter, M., 1984. Cordilleran deformation along the eastern edge of the Calles-San Luis Potosí carbonate platform, Sierra Madre Oriental fold thrust belt, east-central Mexico. *Geological Society of America Bulletin, 95,* 1387 – 1397.

Vogt C., Marquart, G., Kosack, C., Wolf, A., Clauser, C., 2012. Estimating the permeability distribution and its uncertainty at the EGS demonstration reservoir Soultz-sous-Forêts using the ensemble Kalman filter, *Water Resources Research, 48,* W08517, doi: 10.1029/2011WR011673.

Ziagos, J. P., Blackwell, D. D., Mooser, F., 1985. Heat Flow in Southern Mexico and the Thermal Effects of Subduction. *Journal of Geophysical Research, 90,* 5410 – 5420.

Coordination Office, GEMex project

Helmholtz-Zentrum Potsdam
Deutsches GeoForschungsZentrum

Telegrafenberg, 14473 Potsdam

Germany